# Mapping spatially-resolved transcriptomes in systemic sclerosis

Zhijian Li[1,2], Aleix Rius Rigau[3,4], Wenjie Xie[5], Xiaohang Shao[6], Yi-Nan Li[7,8], Alexandru-Emil Matei[7,8], Hejian Zou[9,10,11], Luca Pinello[1,2,12], Jörg H.W. Distler[7,8*], Rui He[5,13*], and Minrui Liang[9,10,11*]

[1]Broad Institute of Harvard and MIT, Cambridge, MA, USA

[2]Molecular Pathology Unit, Center for Cancer Research, Massachusetts General Hospital, Boston, MA, USA

[3]Department of Internal Medicine 3, Rheumatology and Clinical Immunology, Friedrich-Alexander-University Erlangen-Nürnberg (FAU) and University Hospital Erlangen, Erlangen, Germany.

[4]Deutsches Zentrum Immuntherapie (DZI), FAU Erlangen-Nürnberg and University Hospital Erlangen, Erlangen, Germany.

[5]Department of Immunology, School of Basic Medical Sciences, Fudan University, Shanghai, China.

[6]Department of Nephrology and Rheumatology Immunology, Ningbo Medical Center Lihuili Hospital, Ningbo, China.

[7]Clinic for Rheumatology, University Hospital Düsseldorf, Medical Faculty of Heinrich Heine University, Düsseldorf, Germany.

[8]Hiller Research Center, University Hospital Düsseldorf, Medical Faculty of Heinrich Heine University, Düsseldorf, Germany.

[9]Department of Rheumatology, Huashan Hospital, Fudan University, Shanghai, China.

[10]Institute of Rheumatology, Immunology and Allergy, Fudan University, Shanghai, China.

[11]Huashan Rare Disease Center, Huashan Hospital, Fudan University, Shanghai, China.

[12]Department of Pathology, Harvard Medical School, Boston, MA, USA.

[13]National Clinical Research Center for Aging and Medicine, Huashan Hospital, Fudan University, Shanghai, 200040, China.

* Correspondence to Prof. Minrui Liang: mliang10@fudan.edu.cn; Prof. Rui He: ruihe@fudan.edu.cn; Univ. Prof. Dr. med. Jörg H.W. Distler: Joerg.Distler@med.uni-duesseldorf.de;

## Abstract

Systemic sclerosis (SSc) is a prototypical fibrotic disease with high mortality and limited treatment options. Despite advances in single-cell RNA sequencing (scRNA-seq), the comprehensive understanding of cellular heterogeneity and cell-cell interaction within the fibrogenesis microenvironment remains limited. We generated spatially resolved transcriptome maps from healthy and SSc skin and built a scRNA-seq atlas to map the single-cell data to spatial space. This enabled us to identify a fibrotic niche, enriched with fibroblasts and macrophages, which is significantly expanded in SSc and correlated with clinical outcome. We revealed disease-specific cell states of fibroblasts and macrophages, and evaluated their spatial dependency on other cell types. We identified selective expression of ACKR3 in fibroblast progenitors that diminishes with SSc progression, which may serve to regulate CXCL12/CXCR4-mediated macrophage recruitment and fibrotic remodeling. Together, we provided an in-depth description at cellular and spatial level of fine-tuned regulatory events occurring in SSc, offering spatiotemporal insights.

## Introduction

Systemic Sclerosis (SSc), an orphan autoimmune disease, is characterized by the progressive fibrosis affecting skin and multiple organs, holding the highest mortality among all rheumatic diseases[1]. The development of effective therapeutic strategies for SSc is impeded by a lack of comprehensive understanding of its pathogenesis and the limited translatability of current preclinical models. Importantly, studying SSc as a prototypical systemic fibrotic disease could yield new insights into the pathogenesis of fibrotic diseases, and aid in the discovery of novel therapeutic approaches.

SSc is characterized by a complex interplay of features that include vasculopathy, inflammation, and fibrosis. Within this triad, fibroblasts have been recognized as pivotal effector cells in the production of extracellular matrix (ECM), largely contributing to developing fibrotic tissue remodeling in SSc. Fibroblasts sense and receive signaling from

the neighboring cells, which are conveyed and converge to the shared and distinct profibrotic pathways[2]. The coordination of fibroblasts with macrophages can shape their cellular response, therefore orchestrating the initiation or resolution of fibrosis across tissues[3–7]. Beyond the conventional macrophage polarization paradigm, new populations of macrophages have been linked with tissue repair and fibrotic remodeling[3–5,7,8]. For instance, phenotypically distinct macrophages (Lyve1$^{lo}$MHCII$^{hi}$ and Lyve1$^{hi}$MHCII$^{lo}$) manifested specific niche-dependent functional roles in pulmonary and cardiac fibrosis[8]. However, it remains largely unexplored whether and how the spatial neighbourhood in the tissue architecture affects the crosstalk between fibroblast and macrophage subsets, potentially driving fibrotic remodeling in SSc.

Recent studies using single-cell RNA sequencing (scRNA-seq) have provided an unprecedented opportunity to study the molecular mechanisms of SSc at single-cell resolution[9–13]. Pioneering studies have characterized fibroblast types and states in SSc[9,11,13]. While these studies have provided valuable insights, they are significantly constrained by the lack of spatial resolution due to the reliance on disaggregated tissue analysis. We recently demonstrated cellular niches centered around endothelial cells or fibroblasts in SSc using a panel of up to 40 markers through multiplex spatial proteomics[14,15]. Thus, a spatially-resolved characterization of genome-wide transcriptomics of SSc is needed.

In this work, we profiled human skin from SSc patients and healthy controls using spatial transcriptomics (ST) technique based on the 10x Visium formalin-fixed paraffin-embedded (FFPE) platform and spatial enhanced resolution omics sequencing (Stereo-seq)[16]. To increase the cellular resolution of our ST data, we integrated two publicly available scRNA-seq datasets, creating a human skin transcriptome atlas and mapping cell type information onto spatial regions. We validated our results using additional spatial profiling techniques with higher resolution, such as imaging mass cytometry (IMC), as well as time-course experimental skin fibrosis. These approaches enabled us to reveal a detailed characterization of pathological cellular communication between fibroblast and

95 macrophage subsets. This has provided insights into therapeutic target discovery by
96 disrupting disease-driving cellular niches and circuits in SSc.

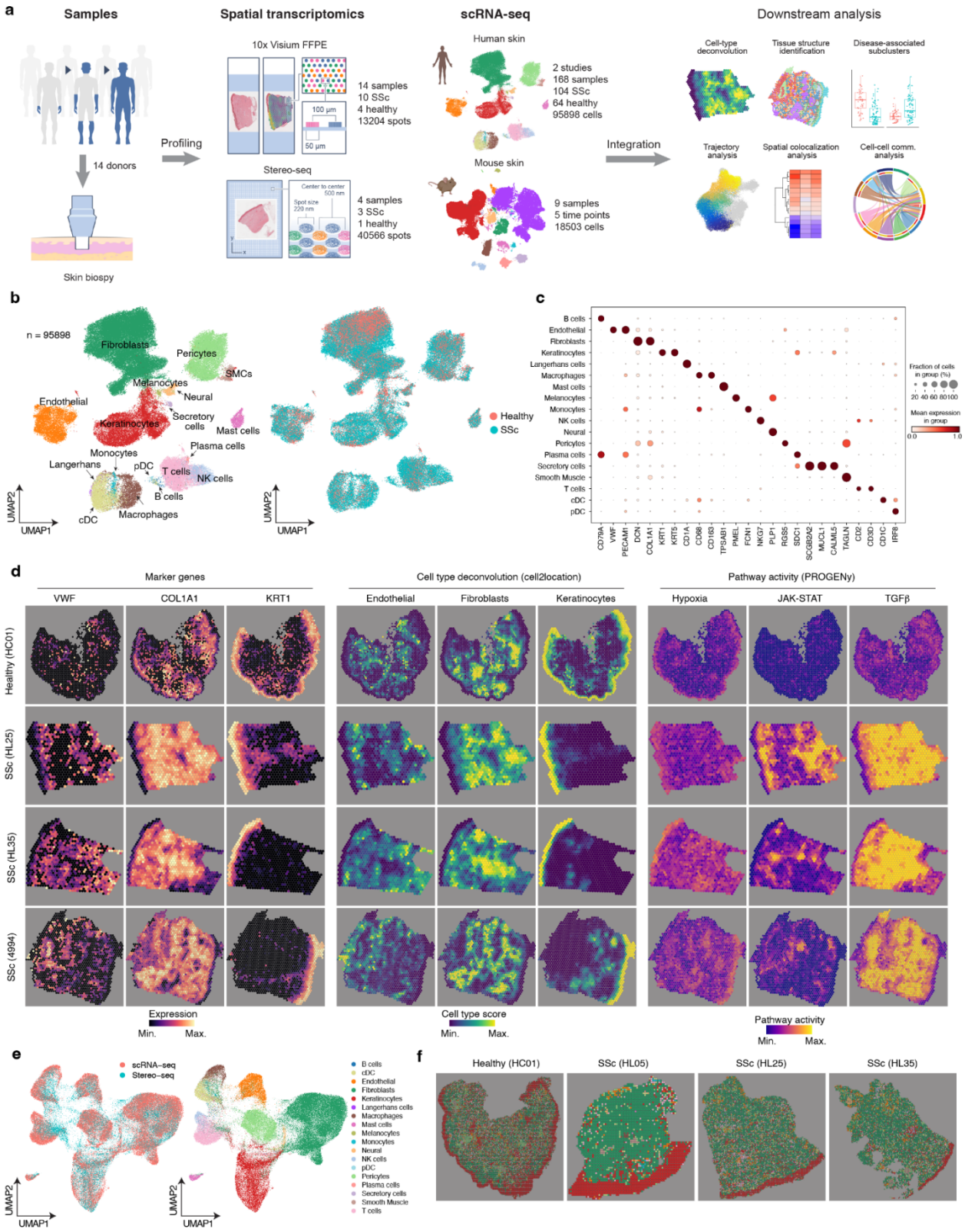


***Fig. 1 Spatial profiling of human skin. a,*** *Overview of experimental design and analysis workflow.* ***b,*** *UMAP showing integrated scRNA-seq datasets as colored by cell types (left) and*

*conditions (right). SSc skin n=104, Healthy skin n=64.* ***c,*** *Dotplot showing gene expression for marker genes. The colors refer to the mean expression of the genes and the dot sizes represent the proportion of cells expressing the marker genes.* ***d,*** *Visualization maps based on 10× Visium. SSc skin n=10, Healthy skin n=4. Left: vWF, COL1A1, and KRT1 gene expressions in spatial transcriptomics data. Middle: representative cell types estimated by cell2location. Right: visualization of pathway activity in spatial space.* ***e,*** *Integration of scRNA-seq and Stereo-seq data colored by protocols (left) and cell types (right).* ***f,*** *Visualization of cell types in spatial space based on Stereo-seq data. SSc skin n=3, Healthy skin n=1. The experiments were performed on adjacent tissue sections to those used for 10× Visium.*

## Results

### Profiling of SSc and healthy skin with spatially-resolved transcriptomics

We collected a total of 14 human skin biopsies from 10 SSc patients enriched for early-stage, diffuse cutaneous involvement, with clinically active disease and 4 sex- and age-matched normal controls (**Fig. 1a**; **Supplementary Table 1**). For each biopsy, we generated spatially resolved transcriptomics (ST) using the 10x Visium platform. After removing low-quality spots across all samples, we retained 13,204 high quality spots with a median detection of 2,265 genes per spot (**Supplementary Fig. 1; Supplementary Table 2**). To enhance spatial resolution, we also performed high-resolution ST profiles on four samples, one from a healthy donor and three from SSc patients, using Stereo-seq. After controlling data quality, we retained 40,566 spots across these samples. We additionally analyzed two scRNA-seq datasets generated from skin tissues of SSc patients (n = 104) and healthy donors (n = 64)[9,10]. The cells were re-annotated for each dataset based on clustering or the original labels (see **Methods**; **Supplementary Fig. 2a-d**). We integrated the scRNA-seq datasets and observed that the same cell types were well-aligned in the UMAP space, which was further confirmed by the cell-type-specific marker genes identified based on the integrated profiles (**Fig. 1b-c; Supplementary Fig. 2e-g**). Together, these data provide a comprehensive multi-modal map of human skin tissues in health and SSc, capturing both spatial and single-cell transcriptomic landscapes.

131 We next deconvoluted the cell-type compositions of each spot in 10x Visium data using
132 the scRNA-seq as reference. The estimated cell type abundances from spatial
133 transcriptomics were generally co-localized with their respective marker genes (**Fig. 1d**).
134 Moreover, we observed that different cell types were mapped to the expected locations.
135 For example, keratinocytes were found localized within the epidermis and surrounding
136 the hair follicle. Endothelial cells were closely associated with vasculature in the dermis.
137 Fibroblasts were distributed throughout the papillary layer and reticular layer of the
138 dermis. We inferred the pathway activity for each spot and observed the enriched
139 expression of genes associated with some well-known pathways, such as Janus kinase
140 signal transducer and activator of transcription protein (JAK-STAT) and transforming
141 growth factor (TGF)-β, reflecting the link between cellular location and the corresponding
142 function (**Fig. 1d**). We transferred the cell type annotation from scRNA-seq to Stereo-seq
143 through data integration (**Fig. 1e**). Spatial visualization of the predicted labels in tissues
144 showed a similar cellular distribution as 10x Visium data (**Fig. 1f**). Collectively, our
145 integrative analyses on spatial transcriptomics and scRNA-seq data enable us to map
146 cell abundance and signaling pathways across zonations in skin samples.
147
148

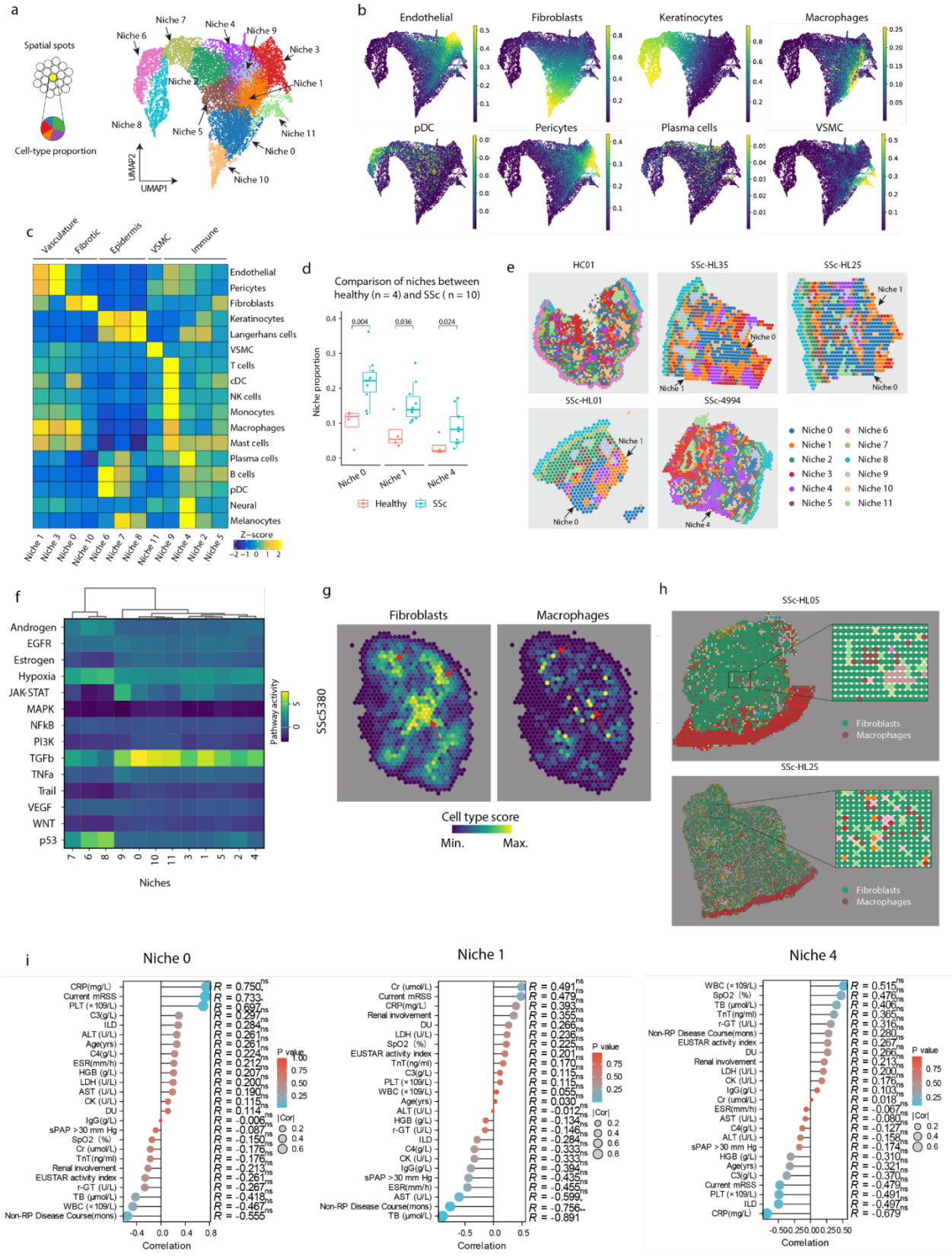


149

150 ***Fig. 2 Characterization of cell-type niches in SSc and healthy skin. a,*** *UMAP showing the*

*integrated spatial data as colored by cell-type niches.* ***b,*** *Visualization of cell type proportion in UMAP space.* ***c,*** *Heatmap showing the enrichment of cell types in niches. Each column represents a niche, and each row represents a cell type. Colors refer to the z-score transformed proportions of each cell type across different niches.* ***d,*** *Boxplot comparing the proportion of each niche between SSc and healthy skin samples. Each dot represents a sample. P-values are calculated using the Wilcoxon rank-sum test (unpaired; two sides).* ***e,*** *Visualization of cell-type niches in spatial space for the healthy and SSc samples using 10x Visium data.* ***f,*** *Heatmap showing pathway activity for each niche.* ***g,*** *Visualization of fibroblasts and macrophages in spatial space using 10x Visium data.* ***h,*** *Visualization of cell types in spatial space using Stereo-seq data.* ***i,*** *Correlations between the proportion of the indicated niches with clinic statistics across all SSc subjects. Statistical significance was determined by the Spearman test for a two-variable correlation. The correlation coefficient r is indicated in figures (* $p < 0.05$). **Abbreviations**: CRP (C-reactive protein), mRSS (Modified Rodnan Skin Score), PLT (platelet count), C3 (complement component 3), ILD (interstitial lung disease), ALT (alanine aminotransferase), C4 (complement component 4), ESR (erythrocyte sedimentation rate), HGB (hemoglobin), LDH (lactate dehydrogenase), AST (aspartate aminotransferase), CK (creatine kinase), DU (digital ulcer), IgG (immunoglobulin G), sPAP (systolic pulmonary arterial pressure), SpO2 (oxygen saturation), Cr (creatinine), TnT (troponin T), EUSTAR activity index (European Scleroderma Trials and Research Group activity index), r-GT (gamma-glutamyl transferase), TB (total bilirubin), WBC (white blood cell count), and Non-RP Disease Course (non-raynaud's phenomenon disease course).*

## Characterization of tissue organization in SSc and healthy skin

To characterize the cellular colocalization events in human skin, we integrated the 10x Visium samples (n = 14) based on the inferred cell-type proportions within each spot (**Supplementary Fig. 3a**). Specifically, we conducted spot deconvolution to determine the proportions of different cell types within each spot, and subsequently clustered the spots based on these identified proportions (**Fig. 2a**). Clustering analysis identified 12 compositionally distinct populations, defined as cell-type niches that represent potential structural building blocks shared across different samples. Visualization of the cell-type abundances and marker genes of these niches revealed that they were strongly associated with the corresponding cell types (**Fig. 2b; Supplementary Fig. 3b-c**). For example, niches 1 and 3 (defined as vasculature niches) were enriched with endothelial

184 cells and pericytes; niches 0 and 10 (defined as fibrotic niches) were enriched with
185 fibroblasts; niches 6, 7 and 8 (defined as epidermis niches) were largely associated with
186 keratinocyte as the representative cell types and along with the infiltration of Langerhans
187 cells; niche 11 was related to vascular smooth muscle cells (VSMC) and therefore defined
188 as a VSMC niche; niche 2, 4, 5, and 9 (defined as immune niches) were related to immune
189 cells (**Fig. 2c**).
190
191 Furthermore, we observed a significant increase in the proportions of three niches (0, 1,
192 and 4) in the SSc skin compared to healthy skin (**Fig. 2d-e; Supplementary Fig. 3d**).
193 Notably, niche 0 was infiltrated with a high prevalence of fibroblasts, macrophages,
194 conventional dendritic cells (cDCs), and mast cells, indicating a potential immune
195 microenvironment within a fibrogenic niche. Niche 1 was characterized by an enrichment
196 of endothelial cells, pericytes, macrophages, cDCs, and mast cells, suggesting a
197 perivascular niche associated with immune cell infiltration in SSc skin. Additionally, niche
198 4 was distinguished by a significant presence of plasma cells, melanocytes, and neural
199 cells (**Fig. 2c**). Moreover, SSc skin exhibited a more reorganized structure, highlighting a
200 tendency towards spatially educated organization, with a dominance in niche distribution
201 (**Fig. 2e**).
202
203 To investigate the featured signaling pathway that characterizes each specific niche, we
204 computed pathway activity. Fibroblast-dominant niche 0 showed the highest activity of
205 the TGF-β signaling pathway. Niche 9, composed of various immune cells, displayed the
206 strongest activity of JAK-STAT signaling (**Fig. 2f**). These findings supported the essential
207 roles of TGF-β and JAK-STAT signaling in the pathogenesis of SSc as expected[2],
208 suggesting a convergence of multiple signaling activities within the structural organization
209 in SSc fibrosis. KEGG pathway enrichment analysis based on marker genes also
210 revealed high activity in the TGF-β signaling in niche 0 (**Supplementary Fig. 3e**).
211
212 Indeed, we observed colocalization of fibroblasts and macrophages in our 10x Visium
213 and Stereo-seq data (**Fig. 2g-h**). To further validate these results, we performed imaging
214 mass cytometry (IMC) and identified the cellular neighborhood (CN) community as

215 described previously[14]. We observed similar niches comprising stromal cells and
216 macrophages (CN8), vascular ECs, and immune cells, including macrophages in CN5
217 (**Supplementary Fig. 4**). To explore the clinical relevance of these niches, we correlated
218 their proportions with clinical data across the SSc samples. Interestingly, we observed a
219 positive Spearman correlation between the proportion of niche 0 and the current total
220 modified Rodnan's skin score (mRSS) ($r$ = 0.721, $p$ = 0.023), C-reactive protein (CRP)
221 levels ($r$ = 0.75, $p$ = 0.066) and platelet counts ($r$ = 0.697, $p$ = 0.031), which are interpreted
222 as clinical indicators for disease severity or activity of SSc (**Fig. 2i**). Additionally, we
223 observed a significant inverse correlation between the proportion of niche 1 and the non-
224 RP disease duration ($r$ = -0.756, $p$ = 0.014). In summary, our spatial multi-omics revealed
225 a distinct structural organization associated with disease outcome of SSc, suggesting a
226 potential coordinated regulation of immune-stromal interactions that may drive the
227 disease progression.
228
229

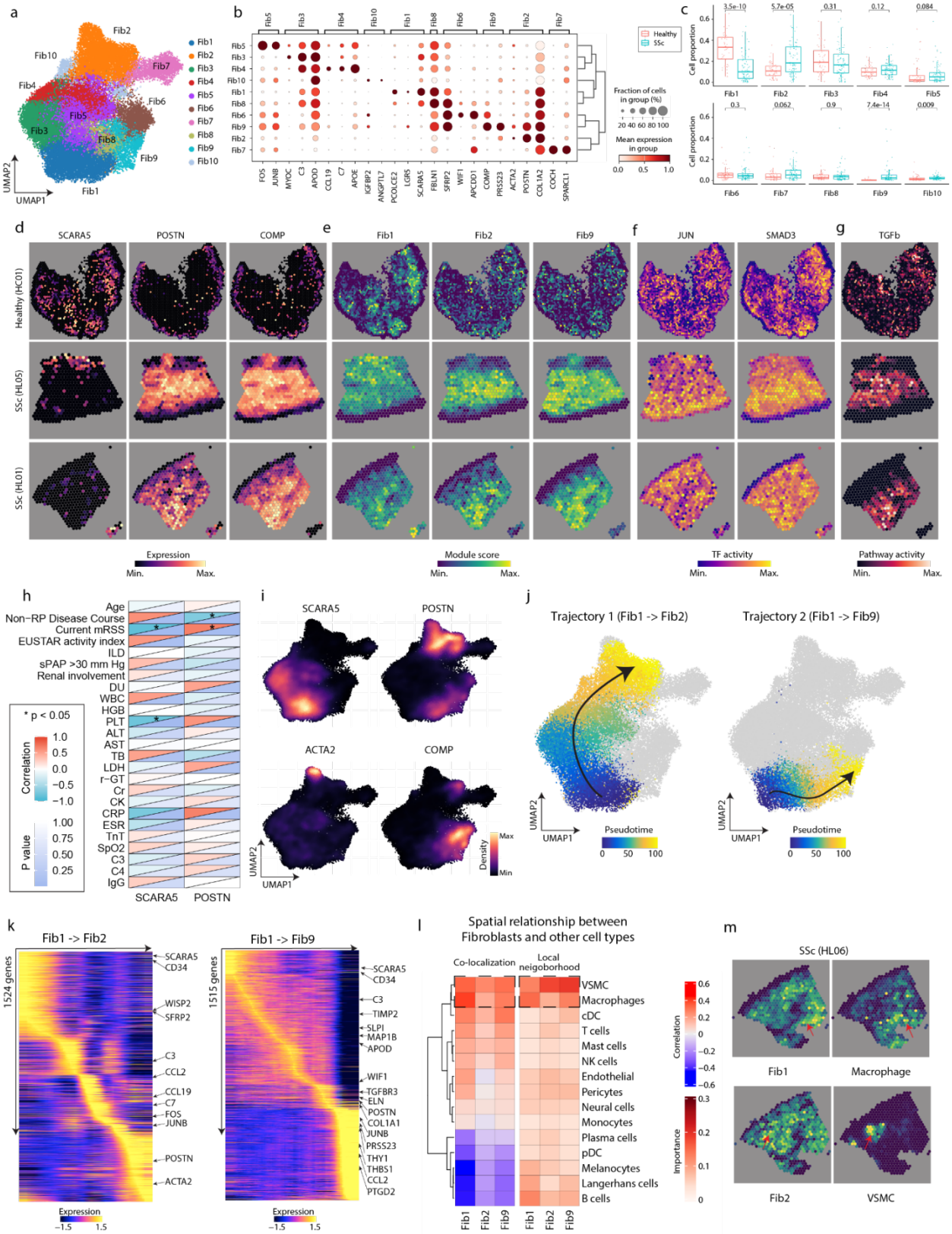
a
Fib1
Fib2
Fib3
Fib4
Fib5
Fib6
Fib7
Fib8
Fib9
Fib10
UMAP1
UMAP2
b
Fraction of cells in group (%)
20 40 60 80 100
Mean expression in group
0.0 0.5 1.0
Healthy
SSc
c
Cell proportion
3.5e-10
5.7e-05
0.31
0.12
0.084
0.3
0.062
0.9
7.4e-14
0.009
d
SCARA5
POSTN
COMP
Healthy (HC01)
SSc (HL05)
SSc (HL01)
e
Fib1
Fib2
Fib9
f
JUN
SMAD3
g
TGFb
Expression
Min.
Max.
Module score
TF activity
Pathway activity
h
Age
Non−RP Disease Course
Current mRSS
EUSTAR activity index
ILD
sPAP >30 mm Hg
Renal involvement
DU
WBC
HGB
PLT
ALT
AST
TB
LDH
r−GT
Cr
CK
CRP
ESR
TnT
SpO2
C3
C4
IgG
* p < 0.05
Correlation
P value
i
SCARA5
POSTN
ACTA2
COMP
Density
Max
Min
j
Trajectory 1 (Fib1 -> Fib2)
Trajectory 2 (Fib1 -> Fib9)
Pseudotime
k
Fib1 -> Fib2
Fib1 -> Fib9
1524 genes
1515 genes
SCARA5
CD34
WISP2
SFRP2
C3
CCL2
CCL19
C7
FOS
JUNB
POSTN
ACTA2
TIMP2
SLPI
MAP1B
APOD
WIF1
TGFBR3
ELN
COL1A1
PRSS23
THY1
THBS1
CCL2
PTGD2
Expression
−1.5
1.5
l
Spatial relationship between Fibroblasts and other cell types
Co-localization
Local neigoborhood
VSMC
Macrophages
cDC
T cells
Mast cells
NK cells
Endothelial
Pericytes
Neural cells
Monocytes
Plasma cells
pDC
Melanocytes
Langerhans cells
B cells
m
SSc (HL06)
Fib1
Macrophage
Fib2
VSMC
Correlation
Importance

230

231 ***Fig. 3 Characterization of fibroblast sub-populations. a,*** *UMAP showing sub-populations of*
232 *fibroblasts based on scRNA-seq data.* ***b,*** *Dot plot showing the marker genes of each subset.* ***c,***
233 *Bar graph comparing the proportion of each fibroblast subset between healthy and SSc samples.*
234 *Each dot represents a sample. P-values are calculated using the Wilcoxon rank-sum test*
235 *(unpaired; two sides).* ***d****, Visualization of SCARA5, POSTN, and COMP expression in spatial*
236 *space.* ***e****, Visualization of module score of Fib1, Fib2, and Fib9 in spatial space.* ***f****, Visualization*
237 *of TF activity of JUN and SMAD3 in spatial space.* ***g****, Visualization of TGF-β pathway activity in*
238 *spatial space.* ***h,*** *Heatmap showing correlations between expressions of SCARA5 and POSTN*
239 *and different clinical outcomes of SSc. The colors in the upper left square represent Spearman's*
240 *r value, while those in the lower right square represent p values (* $p < 0.05$*).* ***i****, Expression of*
241 *SCARA5, POSTN, ACTA2, and COMP overlaying with UMAP.* ***j,*** *UMAP showing the*
242 *differentiation trajectory from Fib1 to Fib2 (left), and Fib1 to Fib9 (right). Colors refer to pseudotime*
243 *points.* ***k,*** *Heatmap showing the gene expression dynamics during the trajectory from Fib1 to Fib2*
244 *(left), and Fib1 to Fib9 (right).* ***l,*** *co-localization between major cell types and fibroblast sub-*
245 *clusters (Fib1, Fib2 and Fib9) as measured within the same spot (left) and neighboring spots*
246 *(right).* ***m,*** *Visualization of the abundance of macrophages and VSMCs and the state scores of*
247 *Fib1 and Fib2 in a representative SSc skin sample.*
248

249 **Characterization of fibroblast sub-clusters in healthy and SSc skin**

250 To investigate the molecular mechanisms driving fibrogenesis in human SSc, we next
251 clustered scRNA-seq data for fibroblasts and identified ten sub-clusters across the
252 datasets and conditions (**Fig. 3a; Supplementary Fig. 5a**). Consistent with previous
253 studies[9,10], we found the corresponding fibroblast populations, including
254 *SCARA5*$^+$/*PCOLCE2*$^+$/*LGR5*$^+$ fibroblasts (Fib1), *MYOC*$^+$/*C3*$^+$/*APOD*$^+$ fibroblasts (Fib3),
255 *CCL19*$^+$/*C7*$^+$/*APOE*$^+$ fibroblasts (Fib4), *SFPR2*$^+$/*WIF1*/*APCDD1*$^+$ fibroblasts (Fib6),
256 *COCH*$^+$/*SPARCL1*$^+$ fibroblasts (Fib7), *COMP*$^+$/*SFPR2*$^+$/*PRSS23*$^+$ fibroblasts (Fib9), and
257 *IGFBP2*$^+$/*ANGPTL7*$^+$ fibroblasts (Fib10) (**Fig. 3b**). Moreover, Fib5 was characterized by
258 the expression of *FOS*, *JUNB*, *JUN* and *FOSB* which were components of activator
259 protein 1 (AP1) known as the core transcription factors in SSc fibrosis[17,18]. Fib1
260 demonstrated the upregulation of *SCARA5*, which has been recently identified as a
261 marker for progenitor fibroblast in human myocardial and kidney fibrosis[19–21]. Fib2 and
262 Fib9 were characterized by the expression of Periostin (*POSTN*), which encodes an
263 extracellular matrix protein that can amplify TGF-β signaling[22,23]. In addition, Fib2 also

264 exhibited a high expression of myofibroblast hallmark *ACTA2*. Together, these suggested
265 that Fib2 and Fib9 as terminally-differentiated ECM-producing myofibroblasts.

266

267 Next, we compared the proportion of each sub-cluster between healthy and SSc samples.
268 We found that Fib1 showed a significant reduction in SSs skin (average fraction = 0.137)
269 compared to healthy skin (average fraction = 0.319) ($p$ = 3.5e-10) (**Fig. 3c**). In contrast,
270 Fib2 exhibited an increase in SSc skin (average fraction = 0.224) compared with that in
271 healthy skin (average fraction = 0.114) ($p$ = 5.7e-05). We also estimated transcription
272 factor (TF) activities for each subset and observed that Fib2 was characterized by high
273 TF activity of the hedgehog transcription factor GLI2 (**Supplementary Fib. 5b**). This
274 convergent driver can mediate Hedgehog pathways in activating fibroblast and promoting
275 fibrosis in SSc[18,24]. Moreover, Fib9 was marked by *SMAD3*, *SMAD4*, and *JUN*, all of which
276 are TGF-β downstream pathways to promote fibrosis. To validate our results, we re-
277 analyzed a bulk RNA-seq dataset from *PRESS* cohort[25] and observed the significant
278 increase of *POSTN* and decrease of *SCARA5* in SSc skin compared with healthy skin[25].
279 An inverse correlation was also observed in the gene expressions between *SCARA5* and
280 *POSTN* (**Supplementary Fig. 5c**). Overall, these findings further supported the potential
281 involvement of *SCARA5*$^+$ and *POSTN*$^+$ fibroblasts in the pathogenesis of SSc.

282

283 We next extended our analysis to spatial transcriptomics data. Visualization and
284 quantification of gene expression showed that *SCARA5* was significantly downregulated
285 in SSc skin, whereas *POSTN* was upregulated in SSc skin (**Supplementary Fig. 5d**).
286 Additionally, *SCARA5* has exhibited distinct spatial enrichment patterns that were
287 mutually exclusive to regions enriched for *POSTN* and *COMP* across multiple samples
288 (**Fig. 3d; Supplementary Fig. 5e**). To characterize the spatial distribution of fibroblast
289 subsets, we calculated module scores of each subset, defined as the average expression
290 of the top 100 marker genes, across spatial spots based on their marker genes. This
291 analysis revealed that Fib2 and Fib9 were spatially colocalized (**Fig. 3e; Supplementary
292 Fig. 5f**). To probe the regulatory networks underlying these subsets, we estimated the
293 activity of TFs and signaling pathways, and observed increased activities of JUN, SMAD3,

294 and the TGF-β pathway, which were closely associated with the spatial localization of
295 Fib2 and Fib9. These findings align with their known pro-fibrotic roles, further confirming
296 the spatial mapping of these sub-clusters (**Fig. 3f-g; Supplementary Fig. 5g-h**). To
297 explore the clinical relevance of these findings, we correlated *SCARA5* and *POSTN*
298 expression with clinical outcomes. Interestingly, *SCARA5* expression negatively
299 correlated with the mRSS, whereas *POSTN* expression positively correlated with mRSS
300 (**Fig. 3h**). Additionally, *SCARA5* showed an inverse correlation with platelet counts, while
301 *POSTN* negatively correlated with non-RP disease duration. These results collectively
302 suggested divergent effects of *SCARA5*$^+$ and *POSTN*$^+$ fibroblasts in SSc fibrosis.

303

304 **Differentiation of *SCARA5*$^+$ *to POSTN*$^+$ fibroblasts in SSc skin**

305 While pioneering studies have identified *SCARA5*$^+$ fibroblasts as myofibroblast
306 progenitors in fibrosis[19–21], their differentiation trajectories have not been constructed yet.
307 To firstly determine if this phenomenon is consistent across different tissues such as SSc
308 skin fibrosis, we analyzed scRNA-seq data from mouse skin challenged by bleomycin
309 (BLM) at various time points (days 3, 7, 14, and 28) and compared them to untreated skin
310 (day 0, steady state)[26]. This analysis identified 14 distinct cell types and nine fibroblast
311 sub-clusters (**Supplementary Fig. 6a-b**). Among these, we found a progressive decrease
312 in *Scara5*$^+$ fibroblasts following BLM treatment, while *Postn*$^+$ fibroblasts substantially
313 increased on days 14 and 28 (**Supplementary Fig. 6c-d**). These temporal changes
314 suggested a potential differentiation process from *Scara5*$^+$ to *Postn*$^+$ fibroblasts.

315

316 Based on these observations and the fact that Fib2 and Fib9 were marked by *POSTN*,
317 we next inferred two pseudo-time trajectories from Fib1 to Fib2 (trajectory 1) and Fib1 to
318 Fib9 (trajectory 2) (**Fig3. i-j**). To characterize transcriptional dynamics during the
319 differentiation, we estimated the expression variation of each gene along the pseudo time
320 and identified 1524 and 1515 genes associated with trajectory 1 and 2, respectively. For
321 trajectory 1, we found many genes were down-regulated during the differentiation,
322 including precursor marker *CD34*[27] and *SFRP2*[9] (**Fig. 3k; Supplementary Fig. 6e**).
323 Moreover, we identified a set of genes, including *C3*, *C7*, *CCL2*, and *CCL19*, that were

324 particularly enriched at the intermediate stage of the trajectory. This suggested a role for
325 chemokine and cytokine signaling, as well as complement system activity, in the
326 differentiation process occurring at this stage. Genes associated with the late stage of
327 this trajectory include *FOS* and *JUNB,* which are involved in the fibrosis-modulatory
328 pathway and have been observed to be activated during the myofibroblast transition
329 process[2]. For trajectory 2, we additionally observed that *TIMP2, TGFBR3* and *APOD* were
330 associated with the intermediate stage. These results revealed distinct gene regulatory
331 networks that are involved in the divergent differentiation of fibroblasts.

332 Of note, Sarthak Sinha et al conducted comparative single-cell multi-omics in reindeer
333 following full-thickness injury and found that the velvet skin regenerates, while the back
334 skin heals by forming a scar[7]. Similarly, in reindeer skin, *SCARA5* gradually decreased
335 but *ACTA2* increased post wound in their back, but not in velvet (**Supplementary Fig.**
336 **7a-e**). This pattern is reminiscent of fibrotic tissue remodeling in human, which indicates
337 the fibroblast dynamic changes could be conserved across species and tissues.

338

339 **Spatial co-localization of fibroblast sub-clusters and other cell types**

340 Apart from highly discordant fibroblast states, the distinct stromal-immune linkages also
341 determine the fibrotic progression. Next, we investigated spatial dependencies between
342 fibroblast subsets and other major cell types to better understand their spatial
343 communications and contributions to fibrotic microenvironments. We conducted spatial
344 colocalization analyses in two distinct proximity areas: 1) co-occurrence within one single
345 spot, determined by Spearman correlation between the module score of each fibroblast
346 sub-cluster and the proportion of each major cell type, and 2) extended neighbourhood
347 within an annular region encompassing up to three surrounding spots for each target spot
348 analyzed with the MISTy pipeline[28]. The results from both approaches were averaged
349 across all samples to identify consistent spatial patterns. We focused specifically on Fib1,
350 Fib2, and Fib9, as they have been demonstrated to exhibit significant alterations in SSc
351 (**Fig. 3c**). Notably, we observed a consistent spatial dependency in both models,
352 characterized by an increased co-occurrence between fibroblast progenitor *SCARA5*$^{+}$
353 Fib1 and macrophages, whereas *POSTN*$^{+}$/*ACTA2*$^{+}$ myofibroblasts (Fib2 and Fib9) were
354 found in proximity to VSMCs (**Fig. 3l-m**). These findings point towards the potential critical

355 role of macrophage in establishing the spatial microenvironment surrounding fibroblast
356 from the early stage.
357
358 **Characterization of macrophage heterogeneity**
359 Beyond the conventional polarization program of macrophage, new subpopulations have
360 been implicated in tissue fibrosis[3–5,29]. They are not the direct source of ECM, but rather
361 a major source of immune dysregulation in fibrotic conditions through release of
362 proinflammatory and profibrotic factors[30]. Nevertheless, the heterogeneity of
363 macrophages and their crosstalk with mesenchymal cells in the diseased context of SSc
364 remain poorly defined. We thus clustered the scRNA-seq data of macrophages and
365 identified three transcriptionally distinct subsets (**Fig. 4a; Supplemental Fig.8a**). We
366 observed one cluster highly expressing proinflammatory cytokine *IL-1β*, as well as
367 *CXCL8*, *CCL3*, *CXCL2* and *PTGS2*, thus termed as proinflammatory macrophages (**Fig.**
368 **4b**). Recent studies have suggested a role of IL-1β$^{+}$proinflammatory macrophages in
369 idiopathic pulmonary fibrosis (IPF), and in cardiac tissue remodeling[3,4]. This subset also
370 highly expresses members of the NR4A subfamily of the nuclear hormone receptor
371 superfamily including *NR4A3, NR4A2 and NR4A1, which* have been identified as
372 immediate early genes in response to various stimuli and considered as promising
373 therapeutic targets due to their significant roles in regulating monocyte differentiation,
374 macrophage activation and inflammatory response[31] and have been linked to the
375 pathogenesis of fibrotic tissue remodeling[32].

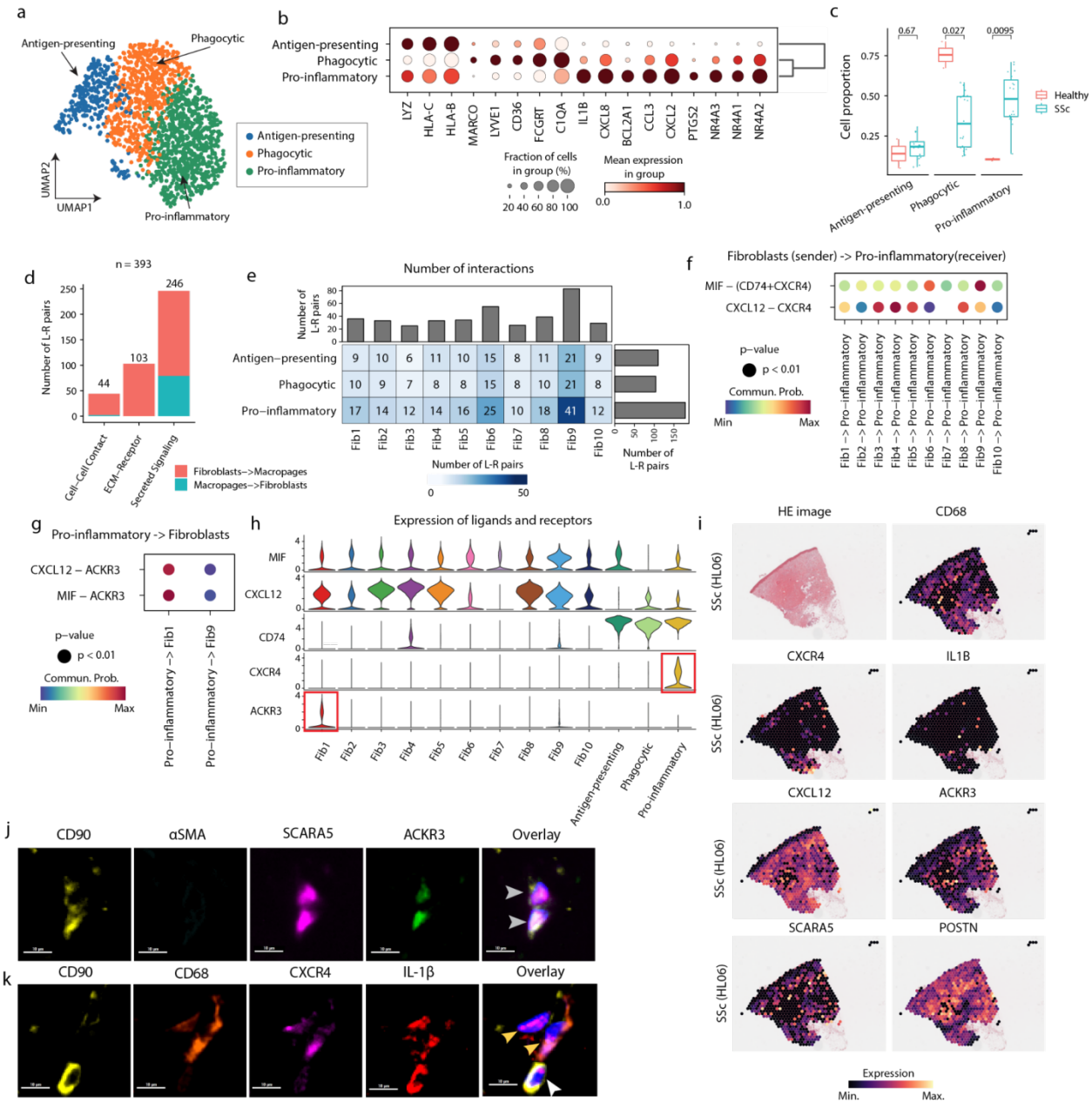


***Fig. 4 Characterization of macrophage sub-clusters.*** ***a****, UMAP showing sub-clusters of macrophages based on scRNA-seq data.* ***b****, Dotplot showing the marker genes for each sub-cluster.* ***c****, Boxplot comparing the proportion of each sub-cluster between healthy and SSc samples. Each dot represents one sample. P-values are calculated using the Wilcoxon rank-sum test (unpaired; two sides).* ***d-e****, Number of significant L-R pairs between the fibroblasts and macrophages.* ***f****, Heatmap showing significant ligand-receptor pairs between fibroblast subsets and proinflammatory macrophages, with fibroblast serving as signaling senders and macrophage*

384 *as receivers. The colors refer to the communication probability and the sizes represent p-values.*
385 ***g**, Heatmap showing significant ligand-receptor pairs between proinflammatory macrophages and*
386 *fibroblast subsets (Fib1, Fib9), as macrophage serving as signaling senders and fibroblast as*
387 *receivers.* ***h**, Violin plot showing the expression of ligands and receptors in scRNA-seq.* ***i**,*
388 *Expression of ligands and receptors in spatial space.* ***j**, Representative images of TSA (Tyramide*
389 *Signal Amplification) staining on the expression of ACKR3 in SCARA5$^{+}$ fibroblast which are*
390 *labeled with CD90 (indicated by grey arrows).* ***k**, Representative images of TSA staining on the*
391 *co-occurrence of fibroblasts (marked by CD90 and indicated by a white arrow) with IL-*
392 *1β$^{+}$macrophages, which are also positive for CXCR4 (indicated by yellow arrows). The staining*
393 *in* ***j*** *and* ***k*** *were performed on adjacent tissue sections to those used for 10× Visium. Horizontal*
394 *scale bars represent 10 μm.*

395 We also identified a sub-cluster characterized by phagocytic markers, including *MARCO*,
396 *LYVE1*, *CD36*, *FCGRT and C1QA*, therefore defined as phagocytic macrophages. The
397 scavenging receptor CD36, known to mediate uptake in macrophage, has been
398 implicated in the pathogenesis of tissue fibrosis[33,34]. *MARCO*, a type II glycoprotein
399 scavenger receptor that binds a broad range of anionic ligands, was found to be
400 upregulated in tissue-resident macrophages and circulating monocytes upon activation.
401 *MARCO*$^{+}$ myeloid cells have been recognized as therapeutic targets for multiorgan
402 fibrosis in SSc[35,36]. LYVE1-expressing macrophage has been demonstrated to form
403 coordinated multi-cellular nest structures that are distributed proximal to vasculature[37].
404 Another subset of macrophage that may be involved in the antigen presentation process
405 is characterized by their overexpression of *HLA-B* and *HLA-C,* hereafter referred to as
406 antigen-presenting macrophages. Indeed, the antigen-presenting macrophage and
407 phagocytic macrophage defined here largely resembled previously identified
408 Lyve1$^{lo}$MHCII$^{hi}$ and Lyve1$^{hi}$MHCII$^{lo}$ macrophages, which are conserved across tissues[8].
409 Notably, the Lyve1$^{hi}$MHCII$^{lo}$ macrophages have been demonstrated to play a critical role
410 in maintaining homeostasis, as depletion of Lyve1$^{hi}$MHCII$^{lo}$ macrophages exacerbated
411 experimental lung and heart fibrosis, along with exacerbated vessel permeability, immune
412 infiltration and collagen deposition[8].

413 The comparison of cell proportion between healthy and SSc samples showed that
414 proinflammatory macrophages were significantly enriched in SSc ($p$ = 0.0095), whereas

415 the abundance of phagocytic macrophages was significantly decreased in SSc samples
416 ($p$ = 0.027) (**Fig. 4c**). We estimated TF activity for each cluster and observed a high
417 activity of REL, RELA, and RELB in proinflammatory macrophages (**Supplementary Fib.**
418 **8b**). These TFs are key members of the NF-κB pathway that regulates immune and
419 inflammatory responses[38], further supporting the functions of proinflammatory
420 macrophages.

421 **Crosstalk between fibroblast and macrophage sub-clusters**

422 Our analysis of ST data revealed a strong spatial association between macrophages and
423 fibroblasts, underscoring their potential functional interplay within the tissue
424 microenvironment (**Fig. 2c; Fig. 3l**). To further investigate the cellular crosstalk between
425 specific macrophage and fibroblast subtypes, we performed a detailed cell-cell
426 communication analysis using CellChat[39] in the scRNA-seq data based on ligand-
427 receptor (L-R) interaction networks. We retained only statistically significant L-R pairs
428 between fibroblast and macrophage sub-clusters, resulting in the identification of 393
429 distinct interactions. These included 246 secreted autocrine/paracrine signaling
430 interactions, 103 ECM-receptor interactions, and 44 direct cell-cell contact-mediated
431 interactions (**Fig. 4d**). This categorization provides a comprehensive view of the diverse
432 modes of communication utilized by these cell types to orchestrate their roles in the tissue
433 microenvironment. Among macrophage subsets, pro-inflammatory macrophages
434 exhibited the highest number of interactions with fibroblast subsets (n = 179 interactions),
435 suggesting that they are central players in fibroblast-mediated signaling (**Fig. 4e**).
436 Particularly, Fib9 emerged as a key fibroblast subtype with the strongest connectivity to
437 macrophages (n = 83 interactions), outpacing other fibroblast subsets in its interaction
438 capacity.
439
440 Visualization of the specific L-R interactions revealed that macrophages receive signals
441 from fibroblasts through multiple signaling pathways, including THBS, MIF, CXCL,
442 LAMININ, and COLLAGEN (**Supplementary Fig. 8c**). Among these interactions, the
443 receptor CXCR4 was observed to interact with fibroblast-derived ligands such as MIF and
444 CXCL12. This interaction suggests a mechanism by which fibroblasts recruit and retain
445 proinflammatory macrophages, thereby sustaining local inflammation and contributing to

446 the progression of fibrosis (**Fig. 4f**). On the other hand, fibroblasts also acted as signal
447 receivers, engaging the receptor ACKR3 to interact with MIF and CXCL12
448 (**Supplementary Fig. 8d; Fig. 4g**). Notably, *MIF* and *CXCL12* were expressed by nearly
449 all subtypes of fibroblasts and macrophages (**Fig. 4h-i**), underscoring their widespread
450 involvement in cellular crosstalk.
451
452 However, the expression of *CXCR4* was specific to proinflammatory macrophages, while
453 *ACKR3* was uniquely expressed in the Fib1 fibroblast progenitor subcluster (**Fig. 4h**). To
454 confirm at the protein levels, we applied Tyramide Signal Amplification (TSA) high-plex
455 immunofluorescence onto adjacent tissue sections. Our TSA staining confirmed the
456 overlapping expression of ACKR3 in SCARA5$^{+}$ fibroblast (**Fig. 4j**). Again, we observed
457 IL-1β$^{+}$ macrophages, which were also positive for CXCR4, closely distributed adjacent to
458 fibroblasts (**Fig. 4k**). Together, these results revealed a highly organized and reciprocal
459 signaling network between fibroblasts and macrophages, underscored by distinct L-R
460 interactions. Of particular interest, the chemokine CXCL12 can bind to its classic receptor
461 CXCR4, a G protein-coupled receptor, facilitating the recruitment of CXCR4$^{+}$ cells, such
462 as proinflammatory macrophages in our case. Alternatively, CXCL12 can interact with its
463 atypical chemokine receptor ACKR3 independent of GPCR mediated signaling. ACKR3
464 is capable of actively internalizing its chemokine ligands CXCL12, through scavenging.
465 This function helps to modulate the availability and gradient of CXCL12 in the extracellular
466 environment[40]. The selective expression of ACKR3 in fibroblast progenitors may indicate
467 an endogenous compensation at an early stage. A dysfunction in this mechanism could
468 lead to the subsequent CXCR4 mediated recruitment of macrophages, during the
469 transition from fibroblast progenitor to myofibroblast over the course of SSc progression.
470

471 **A data-driven model of SSc**

472 Taken together, we proposed a data-driven disease model of SSc based on the results
473 of multi-omics data obtained from SSc, a prototypical systemic fibrotic condition (**Figure**
474 **5**). An imbalance in fibroblast subsets in SSc was characterized by a decrease in
475 *SCARA5*$^{+}$ fibroblast progenitors and an increase in *POSTN*$^{+}$ and *ACTA2*$^{+}$ terminally
476 differentiated myofibroblasts, which promote the excessive ECM deposition. The

477 decreased phagocytic macrophages (Lyve1$^{hi}$MHCII$^{lo}$) may contribute to the impairment
478 of vessel integrity. The infiltration of proinflammatory macrophages (IL-1β$^{+}$) was observed
479 within the fibrotic niche, where they were spatially localized in close proximity to fibroblast
480 subsets. These proinflammatory macrophages were overexpressed with *CXCR4*, which
481 may mediate their recruitment by interacting with *CXCL12*. Additionally, the expression
482 of ACKR3 on fibroblasts, particularly in progenitors under homeostatic conditions, may
483 regulate the local levels CXCL12 by internalizing the ligand, thereby limiting excessive
484 leukocyte recruitment and preventing unwanted tissue inflammation. However, this
485 regulatory mechanism might diminish in effectiveness as progenitor fibroblasts decrease
486 during the progression of SSc, ultimately resulting in uncontrolled CXCL12/CXCR4-
487 mediated inflammatory cell attraction. This regulatory network fosters a shift from tissue
488 homeostasis to a fibrogenic state, driving the progression of SSc. Therefore, the
489 integration of spatial omics with scRNA-seq provides insight into the immune-stromal
490 crosstalk involved in the pathogenesis of SSc.

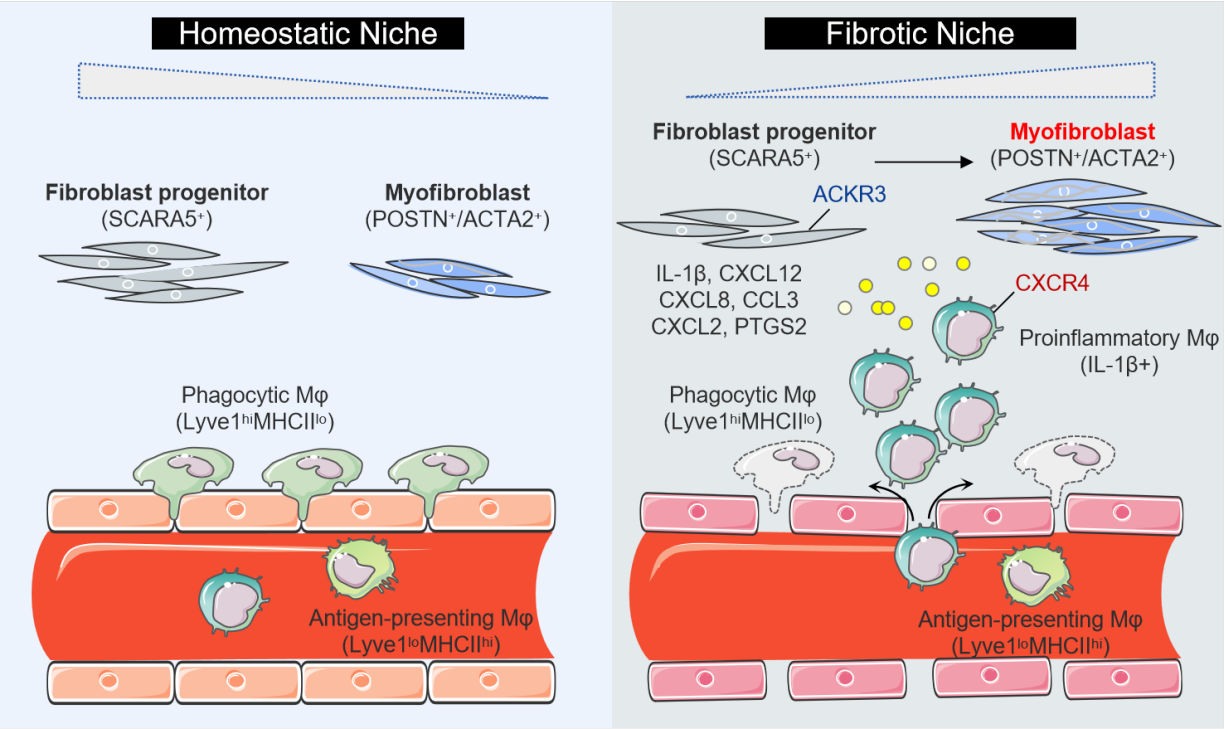


491

492 ***Fig 5. A Data-Driven Model of SSc.*** *Schematic summary illustrates the proposed cellular*
493 *interplay in SSc skin, which leads to a shift from tissue homeostasis to a fibrogenic environment.*
494 *The illustration was created by using images from Servier Medical Art (http://smart.servier.com/),*
495 *licensed under CC BY 3.0 (https://creativecommons.org/licenses/by/3.0/).*

496

497 **Discussion**

498

499 SSc is a multifaceted autoimmune disease characterized by a well-known triad of
500 manifestations: vasculopathy, autoimmunity and fibrosis. In this study, we provided a
501 comprehensive map of the skin ecosystem in SSc using genome-wide spatial
502 transcriptomes based on 10x Visium and Stereo-seq platforms combined with additional
503 scRNA-seq datasets. We identified disease-associated fibroblasts and macrophages and
504 characterized their intricate interplay within niches that potentially drive the transition from
505 a homeostatic to a fibrogenic state. The molecular signatures of cell populations were
506 validated through spatial proteomics, including IMC and TSA. The differentiation
507 trajectory of fibroblasts was cross-validated using time-course bleomycin induced SSc
508 mouse and wound-healing reindeer models. Further investigation into cell-cell
509 communications offered potential for identifying targetable disease-driving molecules for
510 therapeutic intervention.

511

512 Our research aimed to explore the potential to halt the disease progression by interrupting
513 the crosstalk between pathological cells. Spatial transcriptomics provides a unique
514 advantage in examining the structured compartment and the cellular composition and
515 states within specific microenvironments. To overcome the limitations of the 55-um
516 resolution per spot offered by the 10x Visium platform, we employed a higher-resolution
517 spatial transcriptomics technology, FFPE-based Stereo-seq, achieving a resolution of 0.5
518 um per spot. To further validate the genome-wide spatial data, we applied additionally
519 spatial proteomics, including IMC and TSA, which offering the molecular expression and
520 distribution of the identified cells in SSc skin at single-cell level with the resolutions of 1
521 $um^2$ and 0.25 $um^2$ per pixel, respectively. Thus, our study aimed to serve as a
522 comprehensive description of the skin landscape in SSc, revealing potential therapeutic

523 targets.

524

525 We identified distinct niches enriched with fibroblasts and macrophages, showing active
526 TGF-β signaling pathway and correlating with clinical outcomes in SSc. We then homed
527 in on distinct cell phenotypes and spatial relationships of fibroblasts and macrophages
528 within niches. Of note, we discovered a proportional imbalance of fibroblast subsets in
529 SSc, with a clear reduction in SCARA5$^{+}$ progenitor fibroblast and an upregulation in
530 *POSTN*$^{+}$/*ACTA2*$^{+}$ terminally differentiated myofibroblasts compared with healthy controls.
531 SCARA5 positive fibroblasts have been recently reported as myofibroblast progenitors in
532 heart and kidney[19,20,41]. A cross-tissue human fibroblast atlas, derived from 517 human
533 samples encompassing 11 tissue types and diverse pathological states, demonstrated
534 the substantial overlaps among *SCARA5*$^{+}$ fibroblast and progenitor-like fibroblast, as well
535 as between *POSTN*$^{+}$ fibroblast and myofibroblast[42]. Additionally, the dynamic changes of
536 fibroblasts were not only identified through trajectory analysis in human SSc skin, but also
537 validated in time-course models of SSc mouse and wound-healing reindeer using the
538 publicly available datasets[7,26]. These findings indicated that the differentiation from
539 *SCARA5*$^{+}$ fibroblast progenitors to myofibroblasts represents a conserved phenotype
540 across different tissues and species. Targeting the shared mechanism has emerged as
541 a strategy for basket trial design especially for rare diseases that share the same
542 triggering or perpetuating signaling pathways, such as INBUILD study[43]. Of note, we
543 revealed an intense interaction between IL-1β$^{+}$ proinflammatory macrophages and
544 fibroblast subsets in SSc. Infiltrating macrophages activate fibroblasts by secreting IL-1β,
545 whilst systemic IL-1β inhibition or targeted IL-1β deletion in macrophages prevents
546 fibroblast activation[3,4]. Furthermore, we found this crosstalk was predicted to be mediated
547 by the interaction of CXCL12 with CXCR4 in macrophages and ACKR3 in fibroblast
548 progenitors. Indeed, we also found the deregulation of Lyve1$^{hi}$MHCII$^{lo}$ macrophages in
549 SSc, which are known to play a protective role by maintaining vascular integrity and
550 preventing immune cell infiltration in fibrotic conditions[8]. These sequential events such as
551 tissue entry and immune infiltration occuring in SSc may shift the hemostatic condition
552 towards a profibrotic environment. Importantly, the inability to constrain CXCL12
553 overexpression in the milieu through internalization by fibroblast progenitors via ACKR3

554 leads to CXCR4-mediated proinflammatory macrophage recruitment, which is reflective
555 of the fine-tuned regulation by local fibroblasts.

556 In summary, spatial multi-omics combined with scRNA-seq helps to elucidate the
557 entanglement of fibroblasts and macrophages, forming a connectivity network in the
558 pathogenesis of SSc. Within this network, fibroblasts and macrophages with distinct
559 phenotypes contribute to tissue fibrotic remodeling in a coordinated manner. We thus
560 used this strategy to facilitate target discovery, identifying potential intervention axes for
561 fibrosis.

562

563 **METHODS**

564

565 **Human skin biopsy collection and processing**

566 Skin biopsies from 14 SSc subjects and 4 age- and gender-matched healthy controls
567 were obtained and proceeded for spatial transcriptomics using the 10x Visium platform.
568 All skin biopsies of SSc patients were taken on the forearm 15 ± 2 cm proximal from the
569 styloid process of the ulna using disposable biopsy punches (pfm medical, #48301, Gifu,
570 Japan). The epidemiological and clinical features of the SSc patients are presented in
571 Supplemental Table 1. After excluding 2 low-quality SSc samples, as shown in
572 Supplemental Figure 1, we finally included 14 skin biopsies in total, from10 SSc patients
573 and 4 healthy controls. SSc was diagnosed according to the American College of
574 Rheumatology (ACR) /European Alliance of Associations for Rheumatology (EULAR)
575 2013 criteria[44]. In particular, we enrolled SSc patients who had diffused cutaneous
576 involvement and had experienced their initial non-Raynaud's phenomenon symptoms for
577 less than three years. Among the SSc patients, 40% were female and 60% were male.
578 The median age at biopsy of SSc patients was 56.0 years (range 27-73). The median
579 disease duration from the first non-RP symptoms was 8 months (4-48). The median
580 mRSS was 21 (8-41). 40% of SSc patients suffered from interstitial lung disease (ILD).
581 All human studies were approved by the ethical committees of Huashan Hospital of Fudan
582 University. All patients and controls signed a consent form approved by the local
583 institutional review board after informed consent.

584

585 **Spatially profiling human skin with 10x Visium**

586 Formalin-fixed paraffin-embedded (FFPE) skin blocks from a total of 18 subjects were
587 sectioned at 5 um thickness. These sections were transferred to match the 6.5mm$^2$ oligo-
588 barcoded capture areas on the 10× Visium platform (FFPE v2) according to the
589 manufacturer's protocol. Prior to this, archived tissues from paraffin-embedded blocks
590 were tested for RNA quality control (DV200 > 30%), before being mounted on the 10×
591 CytAssist (6.5 mm × 6.5 mm) for library preparation and sequencing (~50,000 reads/spot).
592 Hematoxylin and eosin (H&E) staining was conducted for morphological assessment. The
593 Visium Human Transcriptome Probe Set v2.0 was applied. The final library pool was
594 sequenced on the Illumina Novaseq 6000 instrument using 150-base-pair paired-end
595 reads.

596

597 **Spatially profiling human skin with Stereo-seq**

598 To achieve an enhanced resolution and whole transcriptome in-situ analysis of skin
599 samples, we employed Stereo-seq technology according to the previous protocols[16,45],
600 which enables the spatial detection of transcriptome-wide gene expression at a resolution
601 of 0.5 um. Briefly, 5-um FFPE skin sections from 3 SSc patients and 1 healthy control,
602 which are overlapping with the ones who underwent the examination of 10x Visium, were
603 subjected to adhere to the Stereo-seq chips which have DNA nanoball (DNB) bins with
604 220 nm diameter and a center-to-center distance of 500 nm. After methanol fixation, the
605 formal sections were preceded with ssDNA staining and the adjacent sections with
606 hematoxylin and eosin (H&E) staining for morphological assessment. Next,
607 permeabilization of the tissue was performed to release mRNA. cDNA products are
608 synthesized by reversed transcription. After amplification, DNBs were then generated via
609 rolling cycle amplification (RCA) and loaded onto the patterned chips (65mm×65mm).
610 Next, to determine the distinct DNB-CID sequences at each spatial location, paired-end
611 sequencing was performed on a DNBSEQ-T7 sequencer (MGI Research, Shenzhen,
612 China) with a PE75 sequencing strategy.

613

614 **Processing 10x Visium and Stereo-seq data**

615 For 10x Visium data, we used SpaceRanger software (v2.0.0) to pre-process the raw
616 sequencing data based on the reference genome hg38. For each sample, we filtered the
617 spots by number of detected genes (< 100). For Stereo-seq data, we leveraged nucleic
618 acid staining from the same section to segment cells by projecting the staining image to
619 the Stereo-seq chips. The watershed algorithm was applied to the staining image for
620 single cell segmentations. For each of the segmented cells, UMI from all DNB within the
621 corresponding segmentation were aggregated per-gene and then summed to generate a
622 cell by gene matrix for downstream analysis. To overcome the low RNA capture
623 efficiencies on single DNB spots at a resolution of 500nm, the raw spatial expression
624 matrix was convoluted into larger pseudo-spots with a 50×50 window size (bin50 for
625 short), or more precisely, as 25μm squares. We then filtered the spots by number of
626 detected genes (< 50) and mitochondrial genes (> 10%).
627

628 **Analysis of publicly available scRNA-seq data**

629 To build an atlas of human skin cells, we downloaded scRNA-seq data from Gene
630 Expression Omnibus (GEO) with accession numbers GSE195452 (denoted by
631 Gur2022)[10] and GSE138669 (denoted by Tabib2021)[9]. For the Gur2022 dataset, we only
632 kept the cells from the skin. We further filtered the cells by number of UMIs (< 500),
633 number of detected genes (< 300 or > 5000), and mitochondrial genes (> 30%). We also
634 filtered the genes by the number of cells (n = 100). We re-annotated the cells by merging
635 the 49 original labels to 16 major cell types as follows: Fibroblast (Fibro_ATAC2,
636 Fibro_Bad, Fibro_COCH, Fibro_COMP, Fibro_IGFBP2, Fibro_LGR5, Fibro_MYOC1,
637 Fibro_MYOC2, Fibro_POSTN, Fibro_PTGDS, Fibro_POSTN_PTGDS), T cells
638 (sT_Effector, T_Effector, T_GD, T_Naive, sTreg_CXCR4, sTreg, Treg, sT), NK cells (NK,
639 NK_XCL1, NK_XCL1_CXCR4), cDC (DC, DC_CCL22, DC_CXCL10, DC_XCR1),
640 Macrophages (Mf, Mf_TREM2), Monocytes (Mo_CD16, M_CD16_IL1B, M_IL1B, Mo),
641 Mast cells (bMast_CLC, Mast), B cells (B, B_CXCR4), Pericytes (Peri_RGS5,
642 Peri_TGFBI), Endothelial cells (Vascular_ACKR1, Vascular_RBP7), Keratinocytes
643 (KRT1_KRT10, KRT14_ACTA2, KRT14_S100A2_GJA1). For the Tabib2021 dataset, we
644 filtered the cells by UMIs (<500), number of detected genes (<300 and >5000), and
645 mitochondrial gene expression (> 5%). Since the original annotation was unavailable, we

clustered and re-annotated the cells. This recovered 13 major cell types, among which 10 cell types were also identified by the Gur2022 dataset. To integrate these two datasets, we merged the count matrices and normalized the data using Scanpy[46]. Next, we used the Harmony algorithm[47] to correct the batch effects between the datasets and visualize the integrated cells by UMAP.

**Cell type deconvolution of 10x Visium data**

We used cell2location[48] and the above scRNA-seq data as a reference to estimate cell type composition for each spot in the spatial transcriptomics samples. Specifically, we first identified the signatures of each cell type using the scRNA-seq data based on a Negative binomial regression model after accounting for the batch effects from different datasets. Next, we removed all mitochondrial genes, subsetting the reference data and spatial data using the identified signatures. We ran the function Cell2location (N_cells_per_location=5; detection_alpha=20) to estimate posterior distributions of cell abundance. We normalized the estimated cell type composition for each spot to [0, 1], which was used for visualization and downstream analysis.

**Inference of pathway activity for 10x Visium data**

We used decoupeR[49] (v1.8.0) to infer the pathway and transcription factor activity. Specifically, for each sample, we normalized the expression counts matrix and identified highly variable genes using Scanpy[46]. Next, we obtained a collection of pathways and their target genes using the function get_progeny (organism='human', top=500). The pathway enrichment scores were inferred using the multivariate linear model by running the function run_mlm.

**Integration of scRNA-seq and Stereo-seq data**

We used Seurat (v5.1.0) to integrate the scRNA-seq and Stereo-seq data. Specifically, we merged the Stereo-seq samples and then identified a set of anchors between these two datasets using the function FindTransferAnchors (reduction = "cca") based on the

shared genes (n = 11110). Next, we transferred the cell type labels from scRNA-seq to Stereo-seq data using the function TransferData (weight.reduction = "cca", dims = 1:30). To integrate the data in a common embedding space, we also transferred the batch-corrected PCA components (n = 30) from scRNA-seq to Stereo-seq data with the function TransferData. Next, we run the function RunUMAP to generate a co-embedding space to visualize integrated scRNA-seq and Stereo-seq data.

**Identification of cell-type composition niches in 10x Visium data**

We combined the cell type proportions estimated by cell2location from all samples to. Next, we ran the function neighbors (n_neighbors=30) to create a neighborhood graph of all spatial spots based on the cell type proportions. An UMAP embedding was generated using the function umap with default settings in Scanpy. We clustered the spots with the function leiden (resolution = 0.5), identifying 12 niches. To annotate the niches, we computed the average proportion for each cell type within each niche. We next normalized the values by z-score transformation and clustered the niches using hierarchical approach.

**Sub-clustering of fibroblasts**

We subsetted the fibroblasts and removed the samples with less than 100 cells to allow for robust data integration. Next, we clustered the cells with the Leiden algorithm[50] (resolution =1) based on the harmonized principal components. We removed one population with high mitochondrial genes, resulting in a total of ten clusters identified. The marker genes for each cluster were identified using the function rank_genes_groups (method='wilcoxon') from Scanpy. To map these sub-clusters to spatial space, we selected the top 100 markers for each cluster and then computed module scores using the function AddModuleScore from Seurat[51].

**Analysis of scRNA-seq data from mouse skin**

703 We downloaded scRNA-seq data from the Zenodo data archive
704 (https://zenodo.org/records/7455989). Cells were filtered by the number of UMIs (< 2000
705 or > 40000), number of detected genes (< 200 or > 6000) and fraction of mitochondrial
706 genes (> 5%), retaining 18503 cells. Genes were filtered by the number of cells (< 50).
707 Next, we normalized the count matrix using the functions normalize_total and log1p from
708 Scanpy. Highly variable genes were selected by the function highly_variable_genes. We
709 clustered the cells with the Leiden algorithm (resolution = 0.5) based on the 30 principle
710 components and identified 25 populations which were further grouped into 14 cell types
711 based on their canonical markers. We next subsetted all fibroblasts and clustered the
712 cells using the Leiden algorithm (resolution=0.5), obtaining 10 sub-clusters. We noticed
713 one cluster showing a low number of UMIs and detected genes, presumably
714 corresponding to low-quality cells. We therefore removed this cluster and rename the
715 remaining clusters as Fib1-9.

716

717 **Analysis of scRNA-seq data from reindeer**

718 The scRNA-seq data of full-thickness injuries in skin from reindeer was analyzed with the
719 interface website (www.biernaskielab.ca/reindeer_atlas)[7].

720

721 **Trajectory analysis of fibroblasts**

722 We used ArchR[52] to perform trajectory analysis. Specifically, we inferred two pseudo-time
723 trajectories using the function AddTrajectory to characterize the differentiation processed
724 from Fib1 to Fib2 (denoted by trajectory 1), and from Fib1 to Fib9 (denoted trajectory 2)
725 based on the principle components (n = 30). The trajectory 1 involved six subsets (Fib1,
726 Fib3, Fib5, Fib4, Fib10, and Fib2), and the trajectory 2 included only Fib1 and Fib9. The
727 trajectories were visualized by the function TrajectoryPlot. To identify associated genes
728 for each trajectory, we obtained the expression matrix along the trajectory using the
729 function GetTrajectory (smoothWindow = 11). Next, we visualized the dynamics of gene
730 expression with the function plotTrajectoryHeatmap and selected the top 10% highly
731 variable genes across the trajectory.

732

733 **Spatial relationship analysis between fibroblast subsets and other cell types**

734 We used two approaches to infer spatial relationships between the subsets of fibroblasts
735 and other major cell types. The first approach was based on Spearman correlation
736 between the module score of each subset and the proportion of each major cell type
737 across all spatial spots. This was performed for each 10x Visium sample independently,
738 and results were averaged across all samples. The second approach was based on Misty.
739 Specifically, we usd Misty to build a predictive model using the cell type proportions as
740 features and module scores as target. This allows us to learn the spatial interactions
741 between spots.

742

743 **Sub-clustering of macrophages**

744 We subsetted all macrophages from the integrated scRNA-seq atlas and removed
745 samples with less than 50 cells. Next, clustered the cells using the Leiden algorithm[50]
746 (resolution = 0.3) based on the harmonized principal components, identifying three sub-
747 clusters. The marker genes for each cluster were identified using the function
748 rank_genes_groups (method='wilcoxon') from Scanpy. To map these sub-clusters to
749 spatial space, we selected the top 100 markers for each cluster and then computed
750 module scores using the function AddModuleScore from Seurat[51].

751

752 **Cell-cell communication analysis between fibroblasts and macrophages**

753 We merged the fibroblast and macrophage subclusters to create a Seurat object. Next,
754 we normalized the count matrix using the function NormalizeData from Seurat and
755 identified highly variable genes using the function FindVariableFeatures. We created a
756 CellChat object and grouped the cells based on the sub-clustering results as described
757 above. We selected the database CellChatDB.human and excluded ligand-receptor pairs
758 from non-protein signaling. The cell-cell communication network was inferred using the
759 function computeCommunProb (type = "triMean") and was filtered using the function
760 filterCommunication (min.cells = 10).

761

762 **Imaging mass cytometry (IMC)**

763 We performed data mining using our published IMC dataset[15], which included FFPE skin
764 biopsy sections from 19 SSc patients and 14 matched controls. The IMC panel included
765 up to 38 lanthanide labeled antibodies as well as Iridium 193 and 191 isotopes, which
766 were designed to target epitopes specific for different subsets of endothelial cells,
767 endothelial precursor cells, immune cells and mesenchymal cells, as well as structural
768 markers used for tissue segmentation. Data acquisition was performed on a Helios time-
769 of-flight mass cytometer coupled to a Hyperion Imaging System (Standard Biotools). After
770 single-cell segmentation and data transformation and normalization, we obtained the
771 single-cell dataset with spatial information alongside. We then proceeded with
772 dimensionality reduction, unsupervised clustering, and subsequent cell type annotation.
773 To investigate the local microenvironment of individual fibroblast subpopulations, we
774 identified cellular neighborhoods (CNs) by k-means clustering on the composition of
775 neighboring cells as described[14].

776

777 **Tyramide signal amplification (TSA)**

778 FFPE skin tissue sections obtained from 4 SSc patients and 4 control donors were stained
779 using a TSA system as previously described[15,53]. Briefly, the sections were proceeded
780 with dewaxing, rehydration, and antigen retrieval with Tris-EDTA(pH 9.0) for 15 minutes.
781 Endogenous peroxidase activity was neutralized with 3% $H_2O_2$ for 10 minutes, followed
782 by a 30-minute blocking step with antibody diluent/block buffer (ARD1001EA, AKOYA).
783 Next, sections were incubated for 90 min at room temperature with the following primary
784 antibodies of the indicated dilutions: SCARA5 (ab118894, 1:200, Abcam), CD90
785 (ab226123, 1:200, Abcam), α-SMA (#19245, 1:200, Cell signaling), CD68 (ab192847,
786 1:200, Abcam), IL-1β (ab283818, 1:200, Abcam), CXCR4 (ab181020, 1:200, Abcam) and
787 ACKR3 (20423-1-AP, 1:200, Proteintech). After multiple rounds of signal amplification
788 with Opal fluorophores and subsequent antibody stripping, sections were stained with
789 DAPI. Slides were scanned using a PhenoImager Fusion scanner (Akoya Biosciences)
790 to distinguish the spectra of the different fluorescence channels. All images were captured

791 and presented using the same equipment setting. Merging channels was conducted using
792 ImageJ / Fiji software (Release 2.16.0, https://fiji.sc).

793

794 **References**


795 1. Elhai, M. *et al.* Mapping and predicting mortality from systemic sclerosis. *Ann.*
796 *Rheum. Dis.* **76**, 1897–1905 (2017).
797 2. Distler, J. H. W. *et al.* Shared and distinct mechanisms of fibrosis. *Nat. Rev.*
798 *Rheumatol.* **15**, 705–730 (2019).
799 3. Alexanian, M. *et al.* Chromatin remodelling drives immune cell-fibroblast
800 communication in heart failure. *Nature* **635**, 434–443 (2024).
801 4. Amrute, J. M. *et al.* Targeting immune-fibroblast cell communication in heart failure.
802 *Nature* **635**, 423–433 (2024).
803 5. Mayr, C. H. *et al.* Spatial transcriptomic characterization of pathologic niches in IPF.
804 *Sci. Adv.* **10**, eadl5473 (2024).
805 6. Morse, C. *et al.* Proliferating SPP1/MERTK-expressing macrophages in idiopathic
806 pulmonary fibrosis. *Eur. Respir. J.* **54**, 1802441 (2019).
807 7. Sinha, S. *et al.* Fibroblast inflammatory priming determines regenerative versus
808 fibrotic skin repair in reindeer. *Cell* **185**, 4717–4736.e25 (2022).
809 8. Chakarov, S. *et al.* Two distinct interstitial macrophage populations coexist across
810 tissues in specific subtissular niches. *Science* **363**, eaau0964 (2019).
811 9. Tabib, T. *et al.* Myofibroblast transcriptome indicates SFRP2hi fibroblast progenitors
812 in systemic sclerosis skin. *Nat. Commun.* **12**, 4384 (2021).
813 10. Gur, C. *et al.* LGR5 expressing skin fibroblasts define a major cellular hub perturbed
814 in scleroderma. *Cell* **185**, 1373–1388.e20 (2022).
815 11. Clark, K. E. N. *et al.* Single-cell analysis reveals key differences between early-stage
816 and late-stage systemic sclerosis skin across autoantibody subgroups. *Ann. Rheum.*
817 *Dis.* **82**, 1568–1579 (2023).
818 12. Yin, H. *et al.* Endothelial response to type I interferon contributes to vasculopathy
819 and fibrosis and predicts disease progression of systemic sclerosis. *Arthritis*
820 *Rheumatol.* **76**, 78–91 (2024).

821 13. Ma, F. *et al.* Systems-based identification of the Hippo pathway for promoting fibrotic
822 mesenchymal differentiation in systemic sclerosis. *Nat. Commun.* **15**, 210 (2024).
823 14. Rius Rigau, A. *et al.* Imaging mass cytometry-based characterisation of fibroblast
824 subsets and their cellular niches in systemic sclerosis. *Ann. Rheum. Dis.* (2024)
825 doi:10.1136/ard-2024-226336.
826 15. Rius Rigau, A. *et al.* Characterization of vascular niche in systemic sclerosis by
827 spatial proteomics. *Circ. Res.* **134**, 875–891 (2024).
828 16. Chen, A. *et al.* Spatiotemporal transcriptomic atlas of mouse organogenesis using
829 DNA nanoball-patterned arrays. *Cell* **185**, 1777–1792.e21 (2022).
830 17. Avouac, J. *et al.* Inhibition of activator protein 1 signaling abrogates transforming
831 growth factor β-mediated activation of fibroblasts and prevents experimental fibrosis.
832 *Arthritis Rheum.* **64**, 1642–1652 (2012).
833 18. Bergmann, C. *et al.* Mutual amplification of GLI2/Hedgehog and cJUN/AP1 signaling
834 in fibroblasts in Systemic Sclerosis (SSc) - potential implications for combined
835 therapies. *Arthritis Rheumatol.* (2024) doi:10.1002/art.42979.
836 19. Kuppe, C. *et al.* Decoding myofibroblast origins in human kidney fibrosis. *Nature* **589**,
837 281–286 (2021).
838 20. Kuppe, C. *et al.* Spatial multi-omic map of human myocardial infarction. *Nature* **608**,
839 766–777 (2022).
840 21. Li, Z. *et al.* Chromatin-accessibility estimation from single-cell ATAC-seq data with
841 scOpen. *Nat. Commun.* **12**, 6386 (2021).
842 22. Nanri, Y. *et al.* Cross-talk between transforming growth factor-β and periostin can be
843 targeted for pulmonary fibrosis. *Am. J. Respir. Cell Mol. Biol.* **62**, 204–216 (2020).
844 23. Nanri, Y. *et al.* A positive loop formed by SOX11 and periostin upregulates TGF-β
845 signals leading to skin fibrosis. *J. Invest. Dermatol.* **143**, 989–998.e7 (2023).
846 24. Liang, R. *et al.* The transcription factor GLI2 as a downstream mediator of
847 transforming growth factor-β-induced fibroblast activation in SSc. *Ann. Rheum. Dis.*
848 **76**, 756–764 (2017).
849 25. Skaug, B. *et al.* Global skin gene expression analysis of early diffuse cutaneous
850 systemic sclerosis shows a prominent innate and adaptive inflammatory profile. *Ann.*
851 *Rheum. Dis.* **79**, 379–386 (2020).

852 26. Liang, Y. *et al.* Dynamic pathological analysis reveals a protective role against skin
853 fibrosis for TREM2-dependent macrophages. *Theranostics* **14**, 2232–2245 (2024).
854 27. Nazari, B. *et al.* Altered dermal fibroblasts in systemic sclerosis display podoplanin
855 and CD90. *Am. J. Pathol.* **186**, 2650–2664 (2016).
856 28. Tanevski, J., Flores, R. O. R., Gabor, A., Schapiro, D. & Saez-Rodriguez, J.
857 Explainable multiview framework for dissecting spatial relationships from highly
858 multiplexed data. *Genome Biol.* **23**, 97 (2022).
859 29. Buechler, M. B., Fu, W. & Turley, S. J. Fibroblast-macrophage reciprocal interactions
860 in health, fibrosis, and cancer. *Immunity* **54**, 903–915 (2021).
861 30. Bhandari, R. *et al.* Profibrotic activation of human macrophages in systemic sclerosis.
862 *Arthritis Rheumatol.* **72**, 1160–1169 (2020).
863 31. Boulet, S., Le Corre, L., Odagiu, L. & Labrecque, N. Role of NR4A family members
864 in myeloid cells and leukemia. *Curr. Res. Immunol.* **3**, 23–36 (2022).
865 32. Palumbo-Zerr, K. *et al.* Orphan nuclear receptor NR4A1 regulates transforming
866 growth factor-β signaling and fibrosis. *Nat. Med.* **21**, 150–158 (2015).
867 33. Kwak, D. *et al.* CD36/Lyn kinase interactions within macrophages promotes
868 pulmonary fibrosis in response to oxidized phospholipid. *Respir. Res.* **24**, 314 (2023).
869 34. Pennathur, S. *et al.* The macrophage phagocytic receptor CD36 promotes fibrogenic
870 pathways on removal of apoptotic cells during chronic kidney injury. *Am. J. Pathol.*
871 **185**, 2232–2245 (2015).
872 35. Papazoglou, A. *et al.* Epigenetic regulation of profibrotic macrophages in systemic
873 sclerosis-associated interstitial lung disease. *Arthritis Rheumatol.* **74**, 2003–2014
874 (2022).
875 36. Xu, D. *et al.* PLG nanoparticles target fibroblasts and MARCO+ monocytes to reverse
876 multiorgan fibrosis. *JCI Insight* **7**, (2022).
877 37. Anstee, J. E. *et al.* LYVE-1+ macrophages form a collaborative CCR5-dependent
878 perivascular niche that influences chemotherapy responses in murine breast cancer.
879 *Dev. Cell* **58**, 1548–1561.e10 (2023).
880 38. Liu, T., Zhang, L., Joo, D. & Sun, S.-C. NF-κB signaling in inflammation. *Signal*
881 *Transduct. Target. Ther.* **2**, (2017).
882 39. Jin, S., Plikus, M. V. & Nie, Q. CellChat for systematic analysis of cell-cell

883 communication from single-cell transcriptomics. *Nat. Protoc.* (2024)
884 doi:10.1038/s41596-024-01045-4.
885 40. Cuesta-Margolles, G., Schlecht-Louf, G. & Bachelerie, F. ACKR3 in skin
886 homeostasis, an overlooked player in the CXCR4/CXCL12 axis. *J. Invest. Dermatol.*
887 (2024) doi:10.1016/j.jid.2024.08.022.
888 41. Schreibing, F., Anslinger, T. M. & Kramann, R. Fibrosis in pathology of heart and
889 kidney: From deep RNA-sequencing to novel molecular targets. *Circ. Res.* **132**,
890 1013–1033 (2023).
891 42. Gao, Y. *et al.* Cross-tissue human fibroblast atlas reveals myofibroblast subtypes
892 with distinct roles in immune modulation. *Cancer Cell* **42**, 1764–1783.e10 (2024).
893 43. Flaherty, K. R. *et al.* Nintedanib in progressive fibrosing interstitial lung diseases. *N.*
894 *Engl. J. Med.* **381**, 1718–1727 (2019).
895 44. van den Hoogen, F. *et al.* 2013 classification criteria for systemic sclerosis: an
896 American College of Rheumatology/European League against Rheumatism
897 collaborative initiative: ACR/EULAR classification criteria for SSc. *Arthritis Rheum.*
898 **65**, 2737–2747 (2013).
899 45. Chen, A. *et al.* Single-cell spatial transcriptome reveals cell-type organization in the
900 macaque cortex. *Cell* **186**, 3726–3743.e24 (2023).
901 46. Wolf, F. A., Angerer, P. & Theis, F. J. SCANPY: large-scale single-cell gene
902 expression data analysis. *Genome Biol.* **19**, 15 (2018).
903 47. Korsunsky, I. *et al.* Fast, sensitive and accurate integration of single-cell data with
904 Harmony. *Nat. Methods* **16**, 1289–1296 (2019).
905 48. Kleshchevnikov, V. *et al.* Cell2location maps fine-grained cell types in spatial
906 transcriptomics. *Nat. Biotechnol.* **40**, 661–671 (2022).
907 49. Badia-I-Mompel, P. *et al.* decoupleR: ensemble of computational methods to infer
908 biological activities from omics data. *Bioinform Adv* **2**, vbac016 (2022).
909 50. Traag, V. A., Waltman, L. & van Eck, N. J. From Louvain to Leiden: guaranteeing
910 well-connected communities. *Sci. Rep.* **9**, 5233 (2019).
911 51. Hao, Y. *et al.* Dictionary learning for integrative, multimodal and scalable single-cell
912 analysis. *Nat. Biotechnol.* (2023) doi:10.1038/s41587-023-01767-y.
913 52. Granja, J. M. *et al.* ArchR is a scalable software package for integrative single-cell

914 chromatin accessibility analysis. *Nat. Genet.* **53**, 403–411 (2021).
915 53. Liang, M. *et al.* Identification and validation of anti-protein arginine methyltransferase
916 5 (PRMT5) antibody as a novel biomarker for systemic sclerosis (SSc). *Ann. Rheum.*
917 *Dis.* **83**, 1144–1155 (2024).

918 **Data Availability**

919 The scRNA-seq data for human skin were downloaded from GEO with the accession
920 number GSE195452 (Gur2022) and GSE138669 (Tabib2021). A cross-tissue human
921 fibroblast atlas was analyzed with the interface website http://pan-fib.cancer-pku.cn/
922 (Gao2024). The scRNA-seq data of full-thickness injuries in skin from reindeer was
923 analyzed with the interface website www.biernaskielab.ca/reindeer_atlas (Sinha2022).
924 The scRNA-seq data for mouse skin were downloaded from the Zenodo data archive
925 (https://zenodo.org/records/7455989).
926

927 **Code Availability**

928 The codes used in this study are available on Github:
929 https://github.com/lzj1769/Spatial_SSc_project.
930

931 **Acknowledgment**

932 This study was supported by the Natural Science Foundation of China (NSFC)
933 (82371818) to ML, Joint Sino-German research project from NSFC and Deutsche
934 Forschungsgemeinschaft (DFG, German Research Foundation) (82161138022) to
935 JHWD, HZ and ML, Huashan Cultivation research (30302164001) to ML, Huashan
936 Innovation project (2024CX01) to ML, Shanghai Oriental Youth Talent program
937 ( DFYCQN07) to ML, Rappaport MGH Research Scholar Award to LP.
938

939 **Competing interests**

940 Although no disclosures directly relate to the present study, JHWD has consultancy

relationships with Active Biotech, Anamar, ARXX, AstraZeneca, Bayer Pharma, Boehringer Ingelheim, Callidatas, Celgene, Galapagos, GSK, Inventiva, Janssen, Kyverna, Novartis, Pfizer, Quell Therapeutics and UCB, has received research funding from Anamar, ARXX, BMS, Bayer Pharma, Boehringer Ingelheim, Cantargia, Celgene, CSL Behring, Exo Therapeutics, Galapagos, GSK, Incyte, Inventiva, Kiniksa, Kyverna, Lassen Therapeutics, Mestag, Sanofi-Aventis, RedX, UCB and ZenasBio and is CEO of 4D Science and scientific lead of FibroCure. LP has financial interests in Edilytics, Inc., and SeQure Dx, Inc.

**Author contributions statement**

ML and ZL designed the study. ZL performed all data analysis presented in this work. ZL, ML, ARR, WX, XS, YNL and AEM were involved in acquisition and analysis of data. ZL, ML, RH, LP and JHWD were involved in interpretation of data. ML provided essential samples and resources. All authors were involved in manuscript preparation and proof-reading.

**Supplementary Figures**

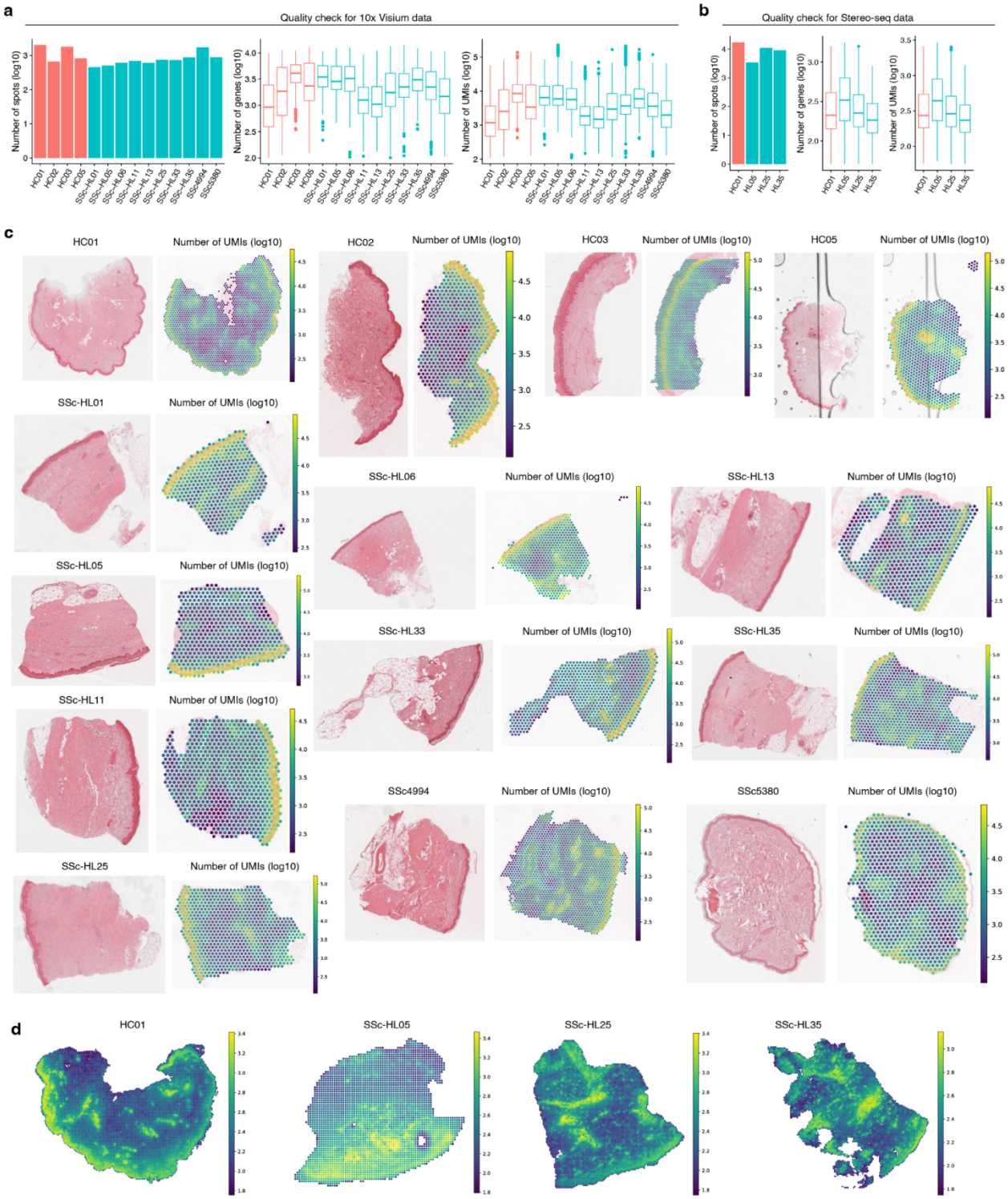


***Supplementary Fig. 1 Quality check of spatial transcriptomics data. a,*** *Left: number of detected spots per sample in 10x Visium data. Middle: number of genes per spot in each sample. Right: number of UMIs in each sample.* ***b,*** *Left: number of detected spots per sample in Stereo-seq. Middle: number of genes per sample. Right: number of UMIs in each sample.* ***c,*** *Visualization*

*of H&E image and number of UMIs in spatial space for 10x Visium data.* ***d,*** *Visualization of number of UMIs in spatial space for Stereo-seq data.*

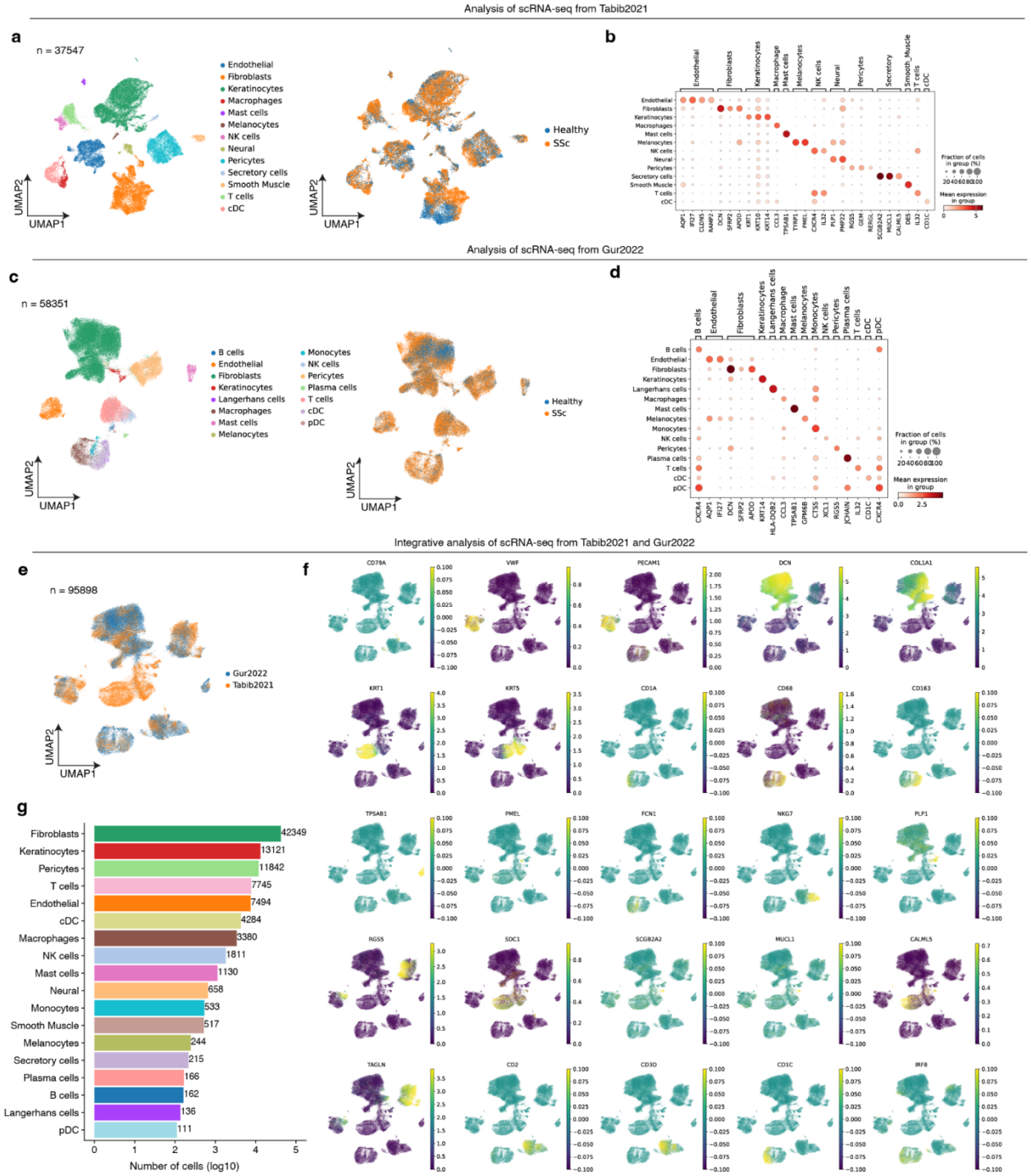


***Supplementary Fig. 2 Analysis of publicly available scRNA-seq data. a,*** *UMAP showing scRNA-seq from the Tabib2021 dataset as colored by cell types and conditions.* ***b,*** *Heatmap*

982 *showing cell-type-specific marker genes.* ***b,*** *UMAP showing scRNA-seq as colored by cell types*
983 *and conditions.* ***c,*** *Same as* ***a*** *for the Gur2022 dataset.* ***d,*** *Same as* ***b*** *for the Gur2022 dataset.*
984 ***e,*** *UMAP showing the integrated scRNA-seq data colored by different datasets.* ***f,*** *Visualization of*
985 *cell-type-specific marker genes.* ***g,*** *Barplot showing number of cells for each cell type.*
986

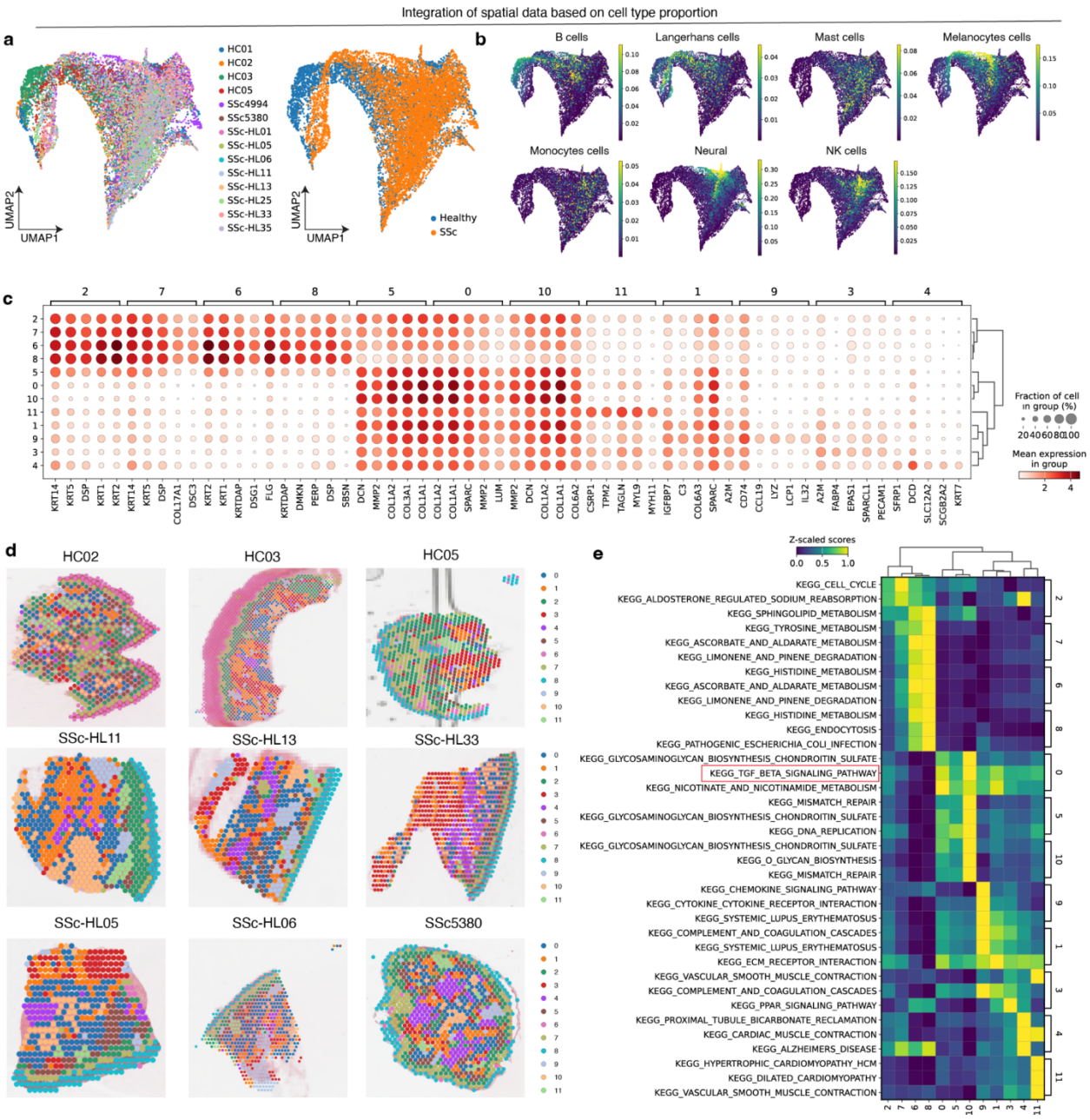


987

988 ***Supplementary Fig. 3 Characterization of cell-type niches in human skin. a-b,*** *UMAP*
989 *embedding of the integrated spatial data as colored by samples, conditions, and the fraction of*
990 *each cell type.* ***c,*** *Marker genes of each cell-type niche.* ***d,*** *Visualization of cell-type niches in*

991 *spatial space.* ***e,*** *KEGG pathway enrichment analysis for each cell-type niche.*

992

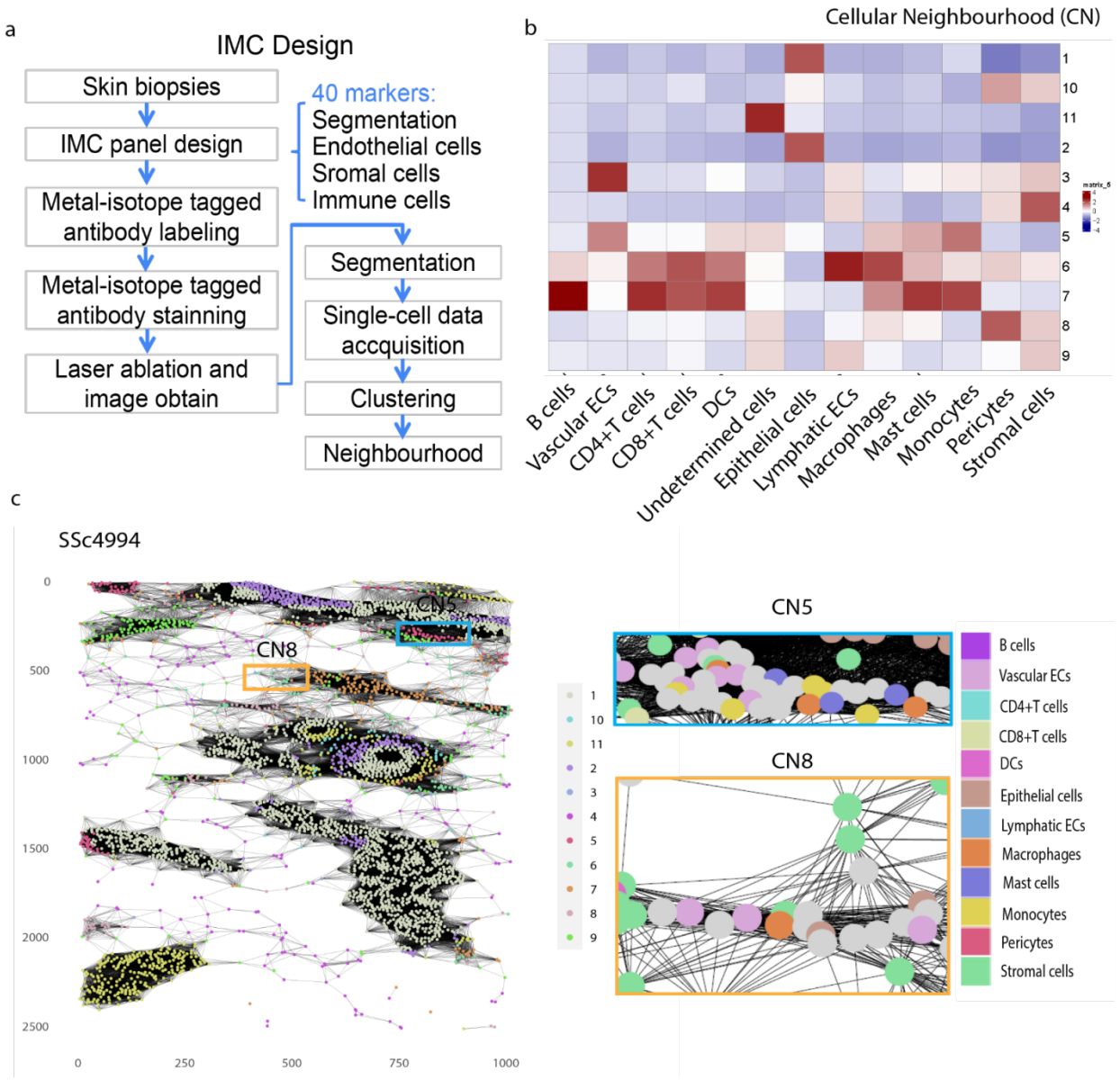


993

994 ***Supplementary Fig. 4 Validation of cellular neighbourhood (CN) by imaging mass***
995 ***cytometry (IMC) in healthy and SSc skin. a****, Study design of IMC, as a validation spatial*
996 *approach. We collected skin biopsies from 19 SSc patients and 14 healthy controls as we*
997 *previously described*[15]*.* ***b****, Heatmap showing the enrichment of cell types in CNs. Each column*
998 *represents a cell type, and each row represents a CN. Colors refer to the proportions of each cell*
999 *type across different CNs.* ***c****, Left: cellular neighborhood (CN) community detected using IMC.*
1000 *Colors refer to cellular clusters. Right: CN5 and CN8 are highlighted and colored by cell types.*

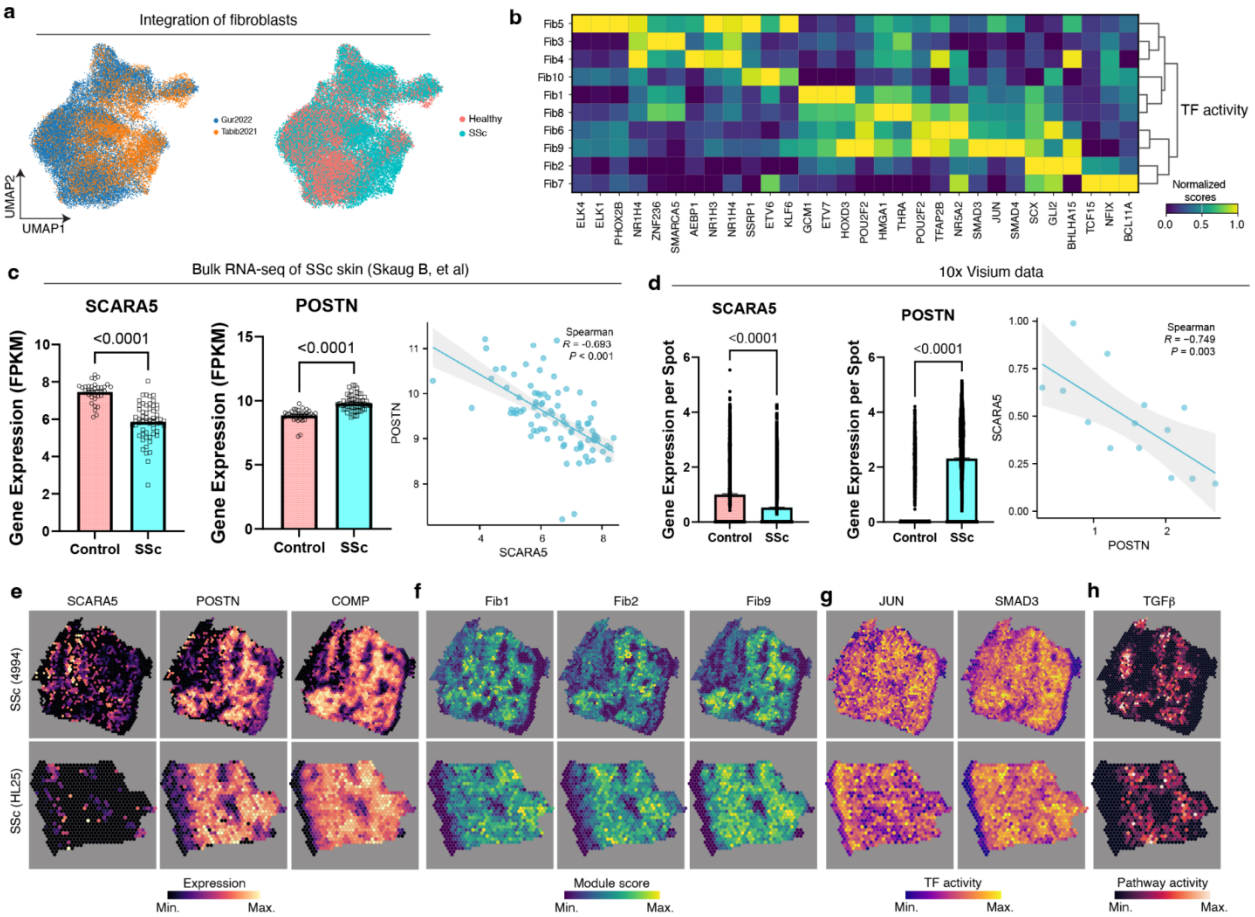


***Supplementary Fig. 5 Sub-clustering of fibroblasts. a,*** *UMAP embedding of the integrated scRNA-seq fibroblasts as colored by datasets and conditions.* ***b,*** *Heamap of top four marker TFs for each sub-cluster-based TF activity score.* ***c,*** *Left: barplot comparing the expression of SCARA5 and POSTN between healthy and SSc conditions using bulk RNA-seq. Right: scatter plot showing the Spearman correlation between SCARA5 and POSTN across patients.* ***d,*** *Left: barplot comparing the expression of SCARA5 and POSTN between healthy and SSc conditions using Visium data. Right: scatter plot showing the Spearman correlation between SCARA5 and POSTN across Visium samples.* ***e-h,*** *Visualization of marker genes, module scores, TF and pathway activities in spatial space.*

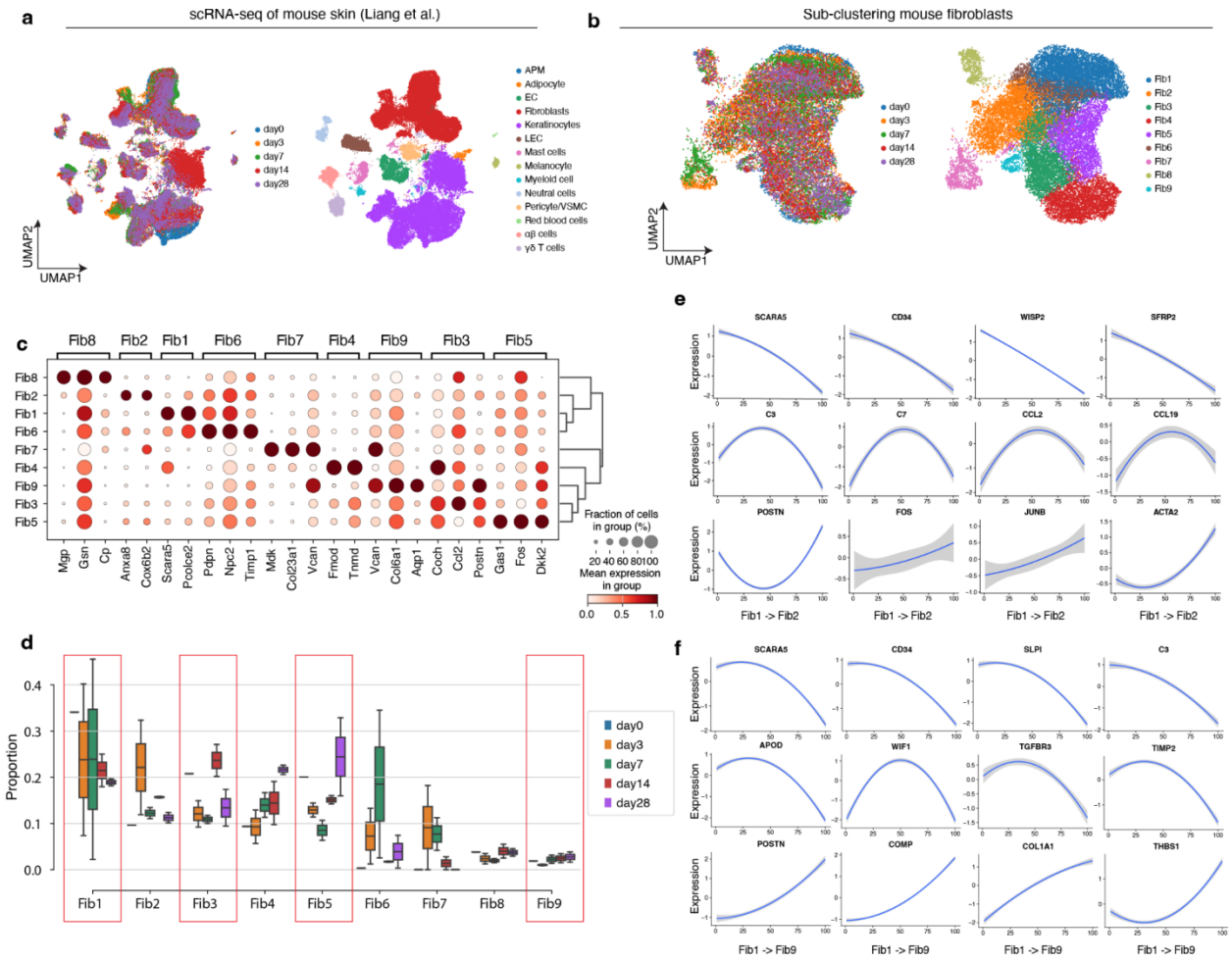


***Supplementary Fig. 6 Trajectory analysis of fibroblast differentiation. a,*** *UMAP of scRNA-seq data from mouse skin[26] colored by time points (left) after bleomycin (BLM) treatment and annotated cell types (right).* ***b,*** *UMAP of fibroblasts colored by time points (left) and sub-clusters (right) and time points (right).* ***c,*** *Dot plots of marker genes for each sub-cluster. The colors refer to the mean expression of the gene, and the size represents the fraction of cells that expressed the gene.* ***d,*** *Box plot showing the fraction of each sub-cluster within different time points.* ***e,*** *Line plot showing expression dynamics of selected genes along the differentiation trajectory from Fib1 to Fib2.* ***f,*** *Line plot showing expression dynamics of selected genes along the differentiation trajectory from Fib1 to Fib9.*

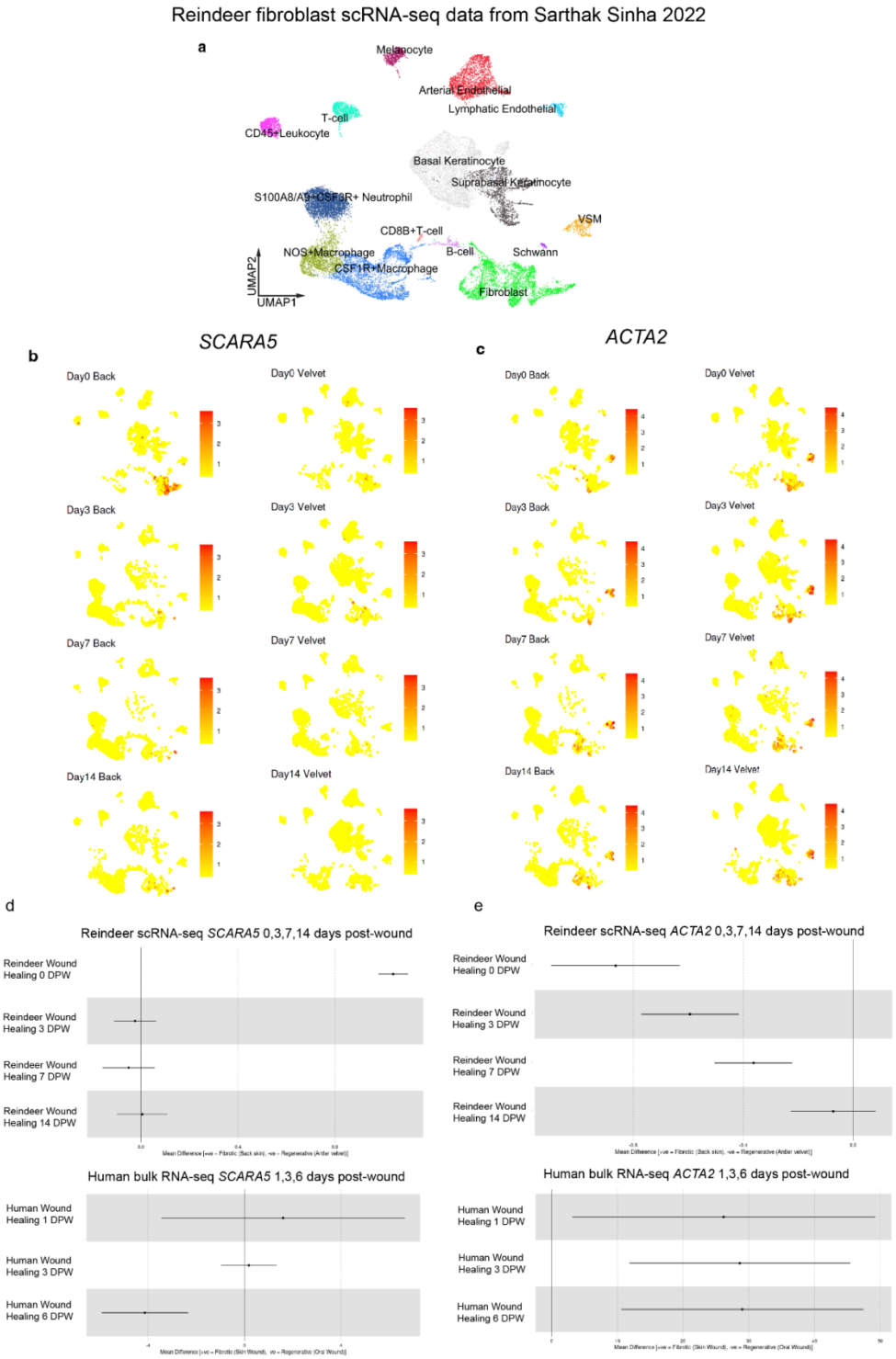


***Supplementary Fig. 7 Cross-Species Validation of Fibroblast Dynamics.*** *Sarthak Sinha et al. utilized single-cell multi-omics to investigate full-thickness skin injuries in reindeer, revealing that their antler skin (velvet) regenerates, while their back skin forms fibrotic scars*[7]*.* ***a****, UMAP of*

*scRNA-seq data from reindeer skin colored by cell type.* ***b,c****, Visualization of SCARA5 (b) and ACTA2 (c) expression in UMAP, showing the gene expression on the back (left) and on the velvet (right).* ***d,e****, Line plot showing expression dynamics of SCARA5 and ACTA2 at the indicated days post wound in reindeer.*

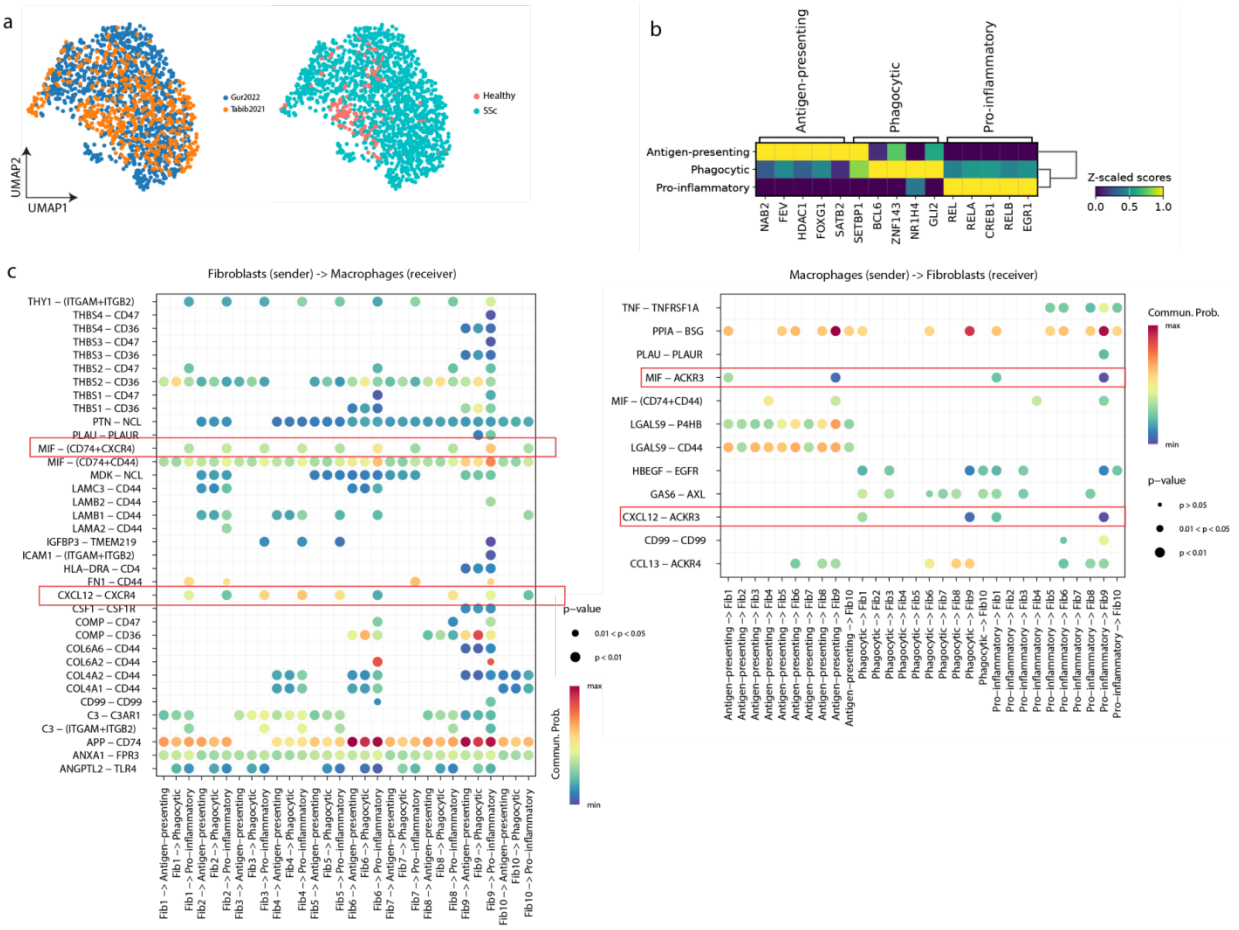


***Supplementary Fig. 8 Sub-clustering of macrophages. a,*** *UMAP showing scRNA-seq of macrophages colored different datasets (left) and conditions (right).* ***b****, Heamap of top four marker TFs for each sub-cluster-based TF activity score.* ***c,*** *Heatmap showing all significant L-R pairs from fibroblasts to macrophages.* ***d,*** *Heatmap showing all significant L-R pairs from macrophages to fibroblasts.*